

© 2023 Junhan Zhao

SENSORLESS CONTROL OF
AN INTERIOR PERMANENT MAGNET SYNCHRONOUS MOTOR
WITH A THREE LEVEL T-TYPE INVERTER

BY

JUNHAN ZHAO

THESIS

Submitted in partial fulfillment of the requirements
for the degree of Master of Science in Electrical and Computer Engineering
with a concentration in Power and Energy Systems
in the Graduate College of the
University of Illinois Urbana-Champaign, 2023

Urbana, Illinois

Adviser:

Professor Kiruba Sivasubramaniam Haran

Abstract

An encoder or resolver is widely utilized for the rotor position and speed feedback in permanent magnet synchronous motor control. However, these sensors sometimes increase the system's cost, size, and complexity. Sensorless control is an alternative strategy, which estimates the rotor position and speed through multi-physical parameters. However, sensorless control requires less harmonic distortion in the motor current and voltage, leading to a large power filter, which further increases the system's size. Therefore, an advanced power electronics typology with less THD is also critical for high accurate sensorless control motor system. Another challenge for sensorless control is the transition between open-loop starting from zero speed and closed-loop control. An unceremonious transition will lead to motor nonalignment and generate significant vibration. The experimental prototype consists of a three-level T-type inverter and a high-power IPMSM, which demonstrated a smooth transition between the open-loop control and closed-loop sensorless control with a speed error of less than $5rpm$ and an accurate sensorless closed-loop control with an error of less than $1rpm$, with the help of a flux linkage observer.

*To Mother and Father
for their unconditional and endless love.*

Acknowledgments

Many thanks to my adviser, Prof. Kiruba Haran, who gave me so much instruction and helped me appreciate the pure beauty of power and electronics. His invaluable guidance, support, and encouragement always accompany me throughout my research journey. Also, thanks to my best friend Shivang Agrawal, who gave me so much help on matters of research and life. Thanks to Kevin, Jodi, Joyce, and so many staff in the power group and POETs who provide so much convenience and allow me to focus on research. Thanks to my parents and friends who endured this long process with me, always offering support and love. And finally, thanks to myself and my 19 years of working.

Table of contents

Chapter 1	Background	1
1.1	Introduction	1
1.2	Sensorless control	3
1.3	Three-level T-type inverter	4
Chapter 2	T-type Inverter and Three-level SVPWM	6
2.1	T-type inverter operation mode	6
2.2	Three-level SVPWM strategy	12
2.3	T-type inverter with SVPWM simulation	16
2.4	Filter Design	20
Chapter 3	Sensorless Control of an IPMSM	25
3.1	IPMSM dynamic model	26
3.2	IPMSM back-EMF SMO observer	28
3.3	SMO sensorless control simulation	34
3.4	IPMSM flux linkage nonlinear observer	38
3.5	Flux observer sensorless control simulation & Comparison between flux observer and SMO	40
3.6	Comparison between SMO and flux-based sensorless control strategy	43
Chapter 4	A starting strategy for sensorless IPMSM	46
4.1	Transition between open and closed-loop control	46
4.2	Simulation of the transition strategy	50
Chapter 5	Experiment	53
5.1	Inverter DC test	54
5.2	Inverter AC test	56
5.3	Flux linkage observer test	59
5.4	Transition and closed loop test	64
Chapter 6	Conclusions	68
References		69
Appendix A	PCB prototype of the T-type inverter	72

Chapter 1

Background

1.1 Introduction

IPMSM stands for Interior Permanent Magnet Synchronous Motor. It is an electric motor that consists of a rotor with permanent magnets embedded inside it and a stator with windings that are excited by an AC voltage. The magnets in the rotor create a magnetic field that interacts with the magnetic field created by the stator windings, generating torque and causing the rotor to rotate. Compared with other electrical machine typologies, IPMSM helps to increase the magnetic flux density, resulting in higher torque and power density. Due to their high efficiency, torque density, and low maintenance requirements, these motors have become increasingly popular in various industrial applications, such as electric vehicles, wind turbines, and robotics.

The term "interior" in IPMSM refers to the placement of the permanent magnets inside the rotor, as shown in Fig. 1.1, as opposed to surface-mounted magnets found in other types of permanent magnet motors (SPMSM). Compared with SPMSM, IPMSM has a larger speed range under constant power output. Furthermore, the interior magnet placement contributes significantly to the magnet's mechanical strength. In addition, magnetic saliency can have the torque generated by both magnetic torque and reluctance torque, while SPMSM relies

only on magnetic torque [1].

The operation of an IPMSM is controlled by an electronic drive that adjusts the frequency

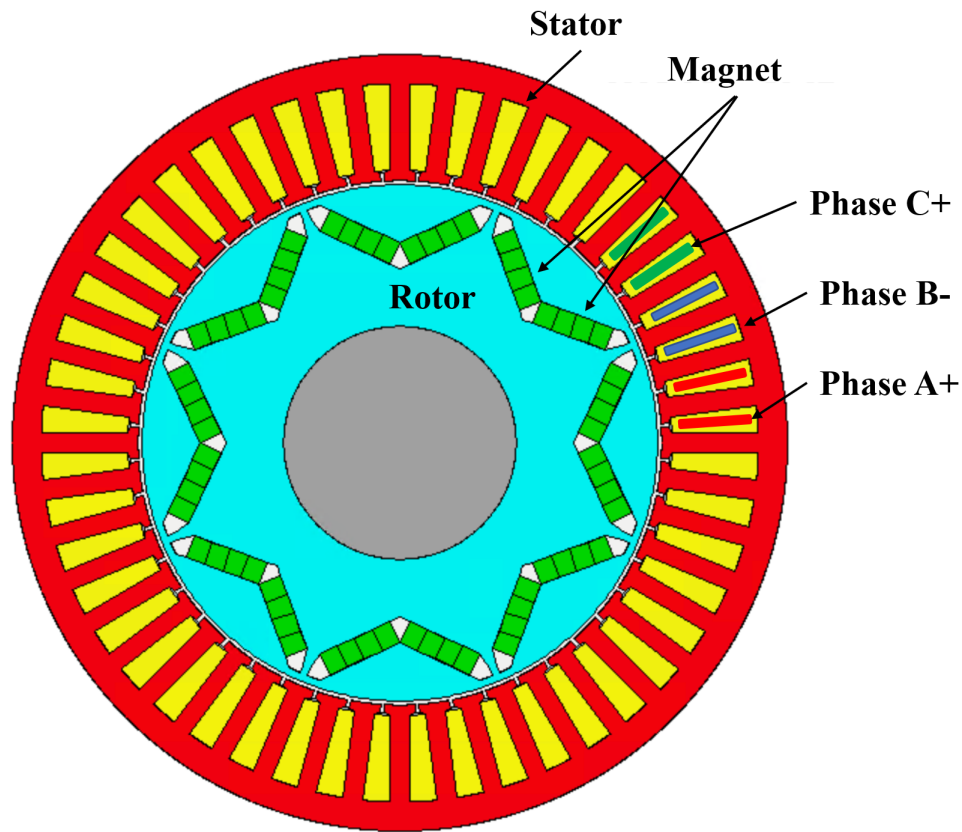


Figure 1.1: IPMSM pole diagram

and amplitude of the AC voltage supplied to the stator windings. The frequency of the voltage determines the speed of the motor, while the amplitude controls the motor's torque. The drive uses feedback from sensors such as encoders or resolvers to monitor the motor's speed and position and adjust the voltage accordingly.

One of the advantages of IPMSMs is their high efficiency due to the reduced losses in the rotor and stator compared to other types of motors. Additionally, using permanent magnets in the rotor eliminates the need for additional field windings, reducing the motor's size and weight. In recent years, researchers have also developed sensorless control techniques for IPMSMs, which allow the motor to operate without using position sensors [2]. These techniques rely on the measurement of the stator currents and voltages to estimate the rotor position and

speed, thereby reducing the cost and complexity of the motor control system.

Overall, IPMSMs are an essential technology for various industrial applications, including electric vehicles, wind turbines, and robotics, due to their high efficiency, power density, and reliability.

1.2 Sensorless control

The control of the motor are typically achieved by using position sensors such as encoders or resolvers, which provide feedback to the controller. However, using position sensors can increase the system's cost, size, and complexity. Sensorless control of IPMSMs is an alternative method to control these motors without position sensors. Instead, it relies on estimating the rotor position and speed using various techniques such as model-based estimation, observer-based methods, and signal injection methods [2]. These methods utilize back-EMF [3], flux linkage [4] from measured stator currents, and voltages to estimate the rotor position and speed. Advanced control techniques such as model predictive control [5] and adaptive control have also been developed for IPMSMs to improve their performance in various applications. Model predictive control uses a model of the motor to predict its behavior and optimize the control inputs. Adaptive control adjusts the control parameters based on the motor's operating conditions to improve its efficiency and performance. The high-frequency signal injection technique is also widely used for sensorless control, especially at starting stage and low-speed range [6].

Sensorless control of IPMSMs has become a popular research area in recent years, due to its advantages, such as reduced cost, improved reliability, and increased robustness. However, it also poses several challenges, such as low-speed operation, model uncertainties, and parameter variations. Researchers are continually developing new methods and algorithms to overcome these challenges and improve the performance of sensorless control of IPMSMs.

Sensorless control needs a highly accurate estimation of rotor position and speed, which is

computed by the voltage and current sampling. However, even the harmonic generated by inverter switching adversely influences the estimation. A power filter is generally utilized to filter some harmonics in motor control, though these filters would lead to some delay in the system. Therefore, an inverter that can generate a more sinusoidal voltage/current significantly contributes to a high-performance sensorless control system, such as a three-level inverter.

1.3 Three-level T-type inverter

Compared with a traditional three-phase full-bridge inverter, a three-level inverter can generate three output voltage levels to decrease the total harmonic distortion, and a T-type three-level inverter is one of them. The T-type inverter is used for voltage regulation and control in various applications, including renewable energy systems, electric vehicles, and industrial motor drives. The T-type topology is named for the shape of the inverter circuit diagram, which resembles the letter 'T'.

Compared to traditional two-level inverters, T-type three-level inverters offer several advantages, including higher output voltage quality, reduced electromagnetic interference, lower total harmonic distortion (THD), and improved thermal management. The inverter achieves these benefits by using a unique configuration of power switches, which allows it to generate three voltage levels from a DC power source with lower switching losses [7].

Research on T-type three-level inverters has focused on developing control strategies and modulation techniques to optimize their performance in different applications. Some of the research topics include improving the inverter's efficiency, reducing its size and cost, enhancing its reliability, and achieving high power density, such as the three-level space vector pulse width modulation (SVPWM) technique [8]. Furthermore, the lower THD can eliminate the power filter utilized for motor drives, especially low-inductance motors, compared with the two-level inverter.

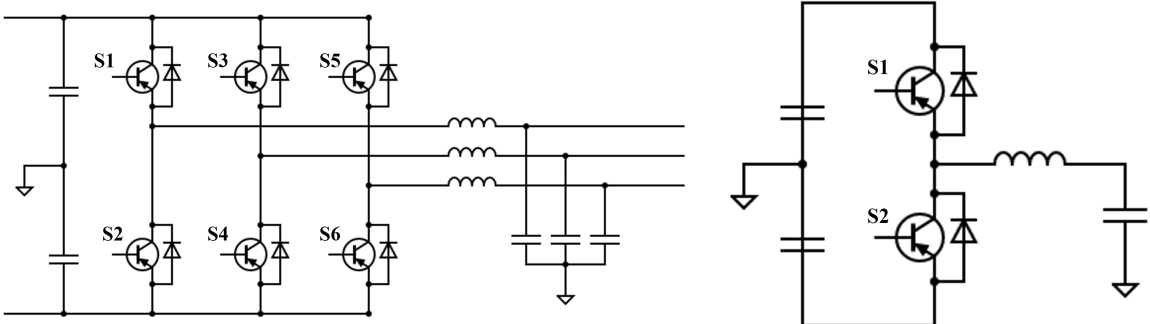
Overall, the T-type three-level inverter is an active research area with significant potential to improve power electronic systems' efficiency, reliability, and performance in various applications, especially motor drives.

Chapter 2

T-type Inverter and Three-level SVPWM

2.1 T-type inverter operation mode

To understand the operation and advantage of a three-level T-type inverter, a traditional two-level inverter is required, as shown in Fig. 2.1(a). The single leg is shown in Fig. 2.1(b).



(a) Two-level, three-phase inverter architecture (b) Two-level, single-phase inverter leg

Figure 2.1: Two-level three-phase inverter architecture and single leg

There are four switch states for the single leg of a two-level inverter, shown in Fig. 2.2. From the switches states and current flowing paths of a two-level inverter, it is necessary for each switching device to block the total DC link voltage between DC+ and DC-. In

low-voltage systems, this can be easily accomplished using standard Si-IGBTs. However, increasing the DC link voltage to improve power throughput without raising the current has become a common trend in power electronics. This increase in voltage places a limit on the supported voltage ranges due to the aforementioned limitation.[9]

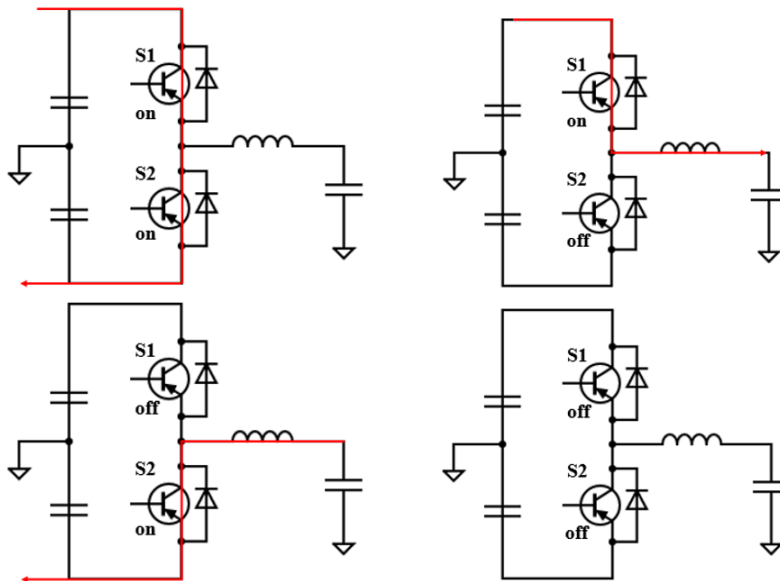
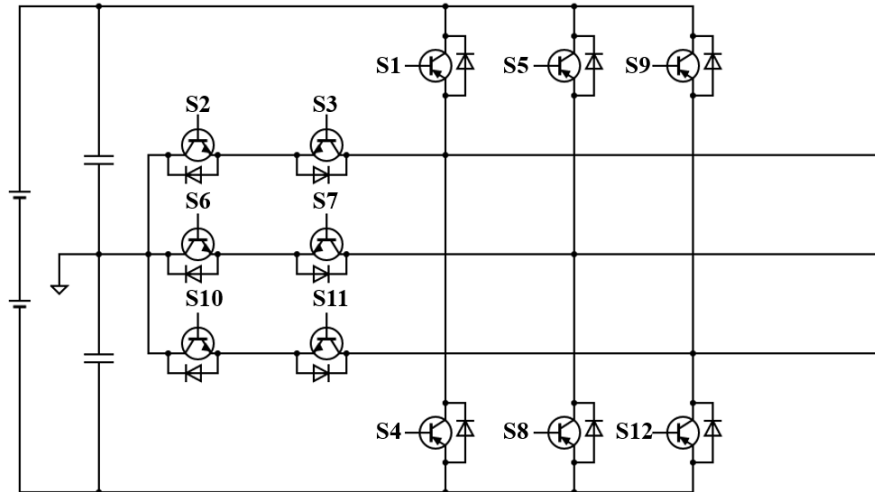


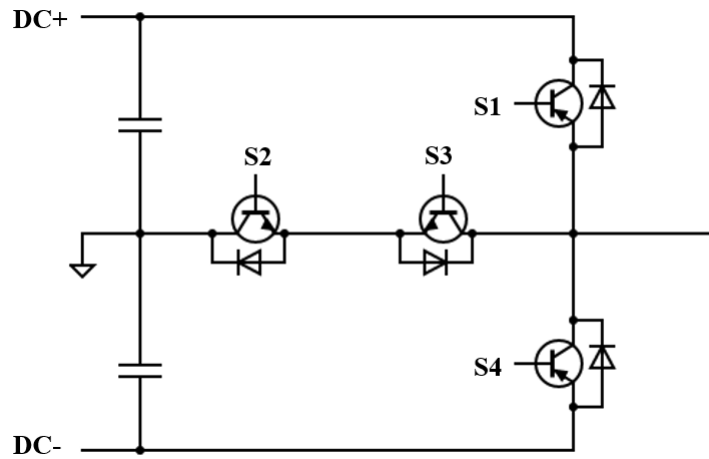
Figure 2.2: Switch states for a two-level inverter

Furthermore, raising the voltage leads to greater switching losses in traditional IGBTs. Even if they are capable of withstanding higher voltages, the high $\frac{dV}{dt}$ aggravates the issue, especially when we want to increase the switching frequency. These two drawbacks of two-level inverters promote the development of the three-level inverter.

A typical three-level inverter is a T-type inverter, which inserts two switching devices between the switch node and the neutral point of the DC links; therefore, each leg of a T-type inverter consists of two half-bridge IGBTs and two neutral point IGBTs, and this configuration also enables both devices to share a standard bias supply, as the neutral point voltage is identically referenced [10]. Fig. 2.3(a) shows the architecture of a T-type inverter. And to aid in comprehending the advantages of the design, the inverter has been simplified to a single leg, as shown in Fig. 2.3(b).



(a) Three-Level T-Type, Three-Phase Inverter Architecture



(b) Three-Level T-Type, single-phase inverter leg

Figure 2.3: Three-Level T-Type, three-phase inverter architecture, and single leg

A single leg has three switch states $DC+$, N , and $DC-$, which can be achieved by closing $Q1$ and $Q2$, closing $Q2$ and $Q3$, and closing $Q3$ and $Q4$. The state transformations of switches with different current directions are shown below.

When $Q1$ and $Q2$ are closed, the leg gives a $DC+$ output with current flowing out from the system. To transition to the N state, $Q1$ is opened, then $Q3$ is closed, which allows the current to flow out from the neutral point, as shown in Fig. 2.4.

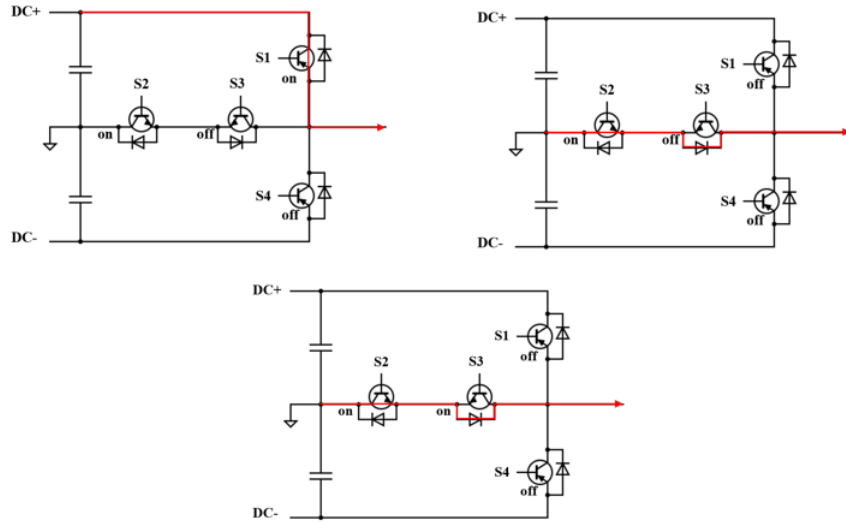


Figure 2.4: Transition from DC+ to N with positive current

When Q2 and Q3 are closed, the leg gives an N output with current flowing out from the system. To transition to the DC+ state, Q3 is opened, then Q1 is closed, which allows the current to flow out from the DC+, as shown in Fig. 2.5.

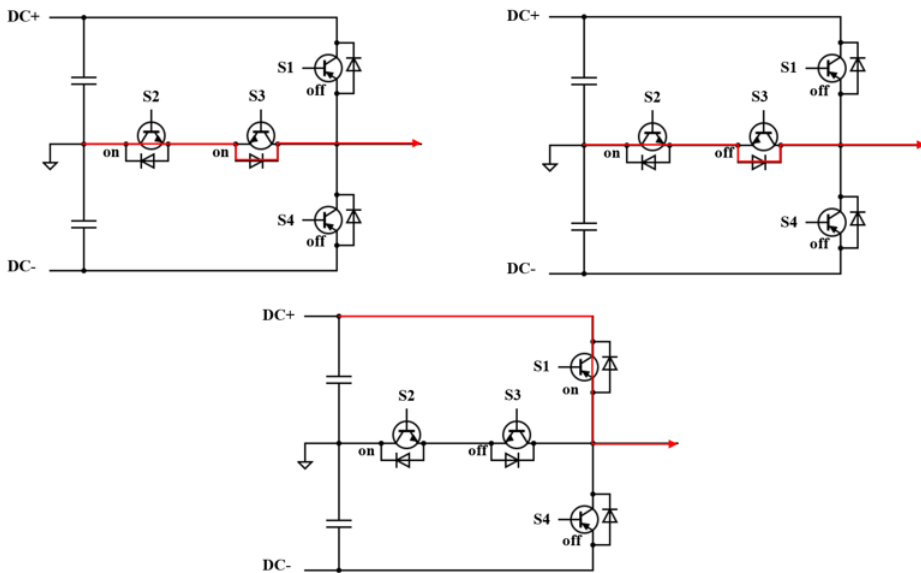
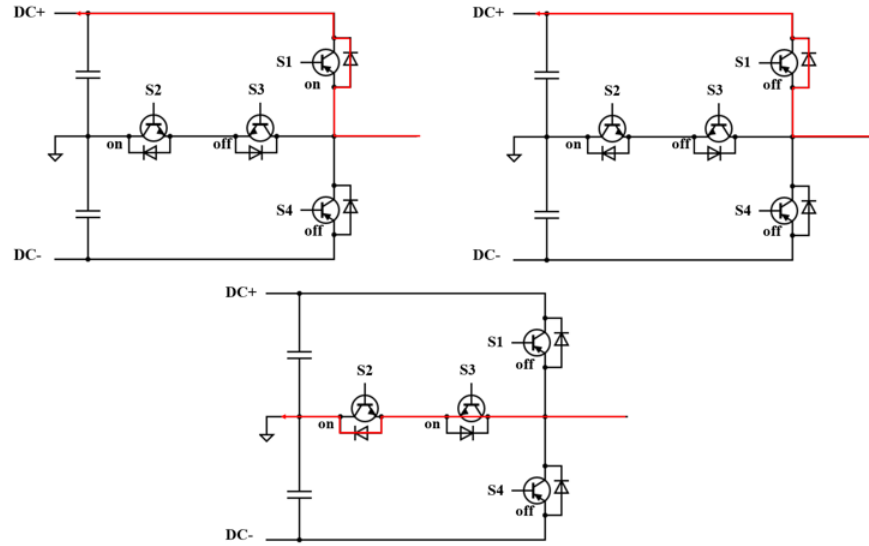
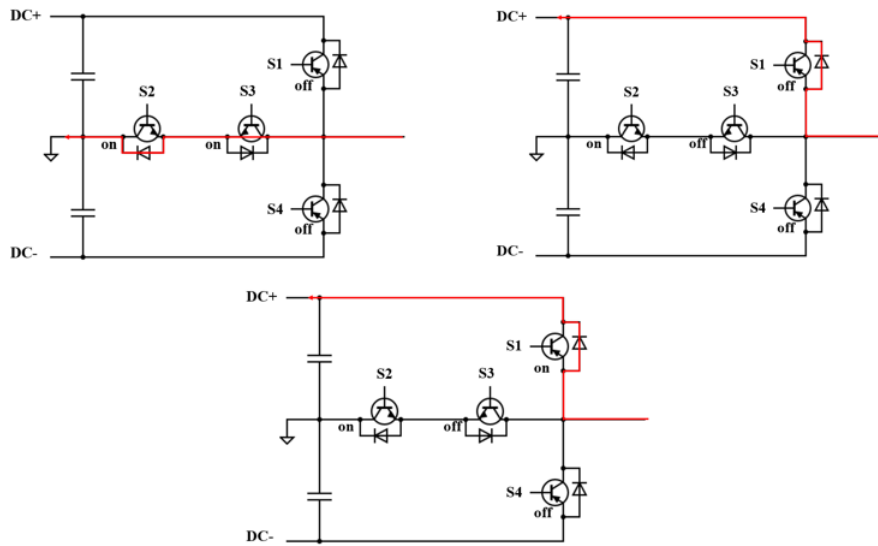


Figure 2.5: Transition from N to DC+ with positive current

For negative current, the switch sequence is the same. The transition from DC+ to N and N to DC+ with negative current is shown in Fig. 2.6(a) and Fig. 2.6(b).



(a) Transition from DC+ to N with positive current



(b) Transition from N to DC+ with positive current

Figure 2.6: Transition between DC+ and N with negative current

This transition scheme offers an additional benefit: devices Q2 and Q3 are never active at the same time. This helps to minimize the voltage stress on these devices and reduces the power rating of the bias supply needed to drive them effectively. However, as in the

traditional architecture, Q1 and Q4 still need to block the full DC link voltage. To use a higher DC bus voltage, full-voltage FETs are still required here [10].

In Fig. 2.3(a), Q1 and Q3 are complementary, similarly, Q2 and Q4 are complementary. Therefore, we can have the terminal output level corresponding to different switch states as Table. 2.1.

Table 2.1: Three terminal voltage output level with different device states

Symbol	Switch state				Terminal voltage
	Q1	Q2	Q3	Q4	
P	ON	ON	OFF	OFF	DC+
O	OFF	ON	ON	OFF	0
N	OFF	OFF	ON	ON	DC-

U_{dc} is the DC bus link voltage, and $DC+ = U_{dc}/2$.

Based on the three levels of each phase, there are totally of 27 states, which is corresponding to 27 voltage vectors, where 24 of them are working vectors, while rest of them are zero vectors. Based on the magnitude of these vectors, we can classify them into four categories:

- Zero vector: the magnitude of zeros vectors are zero, including PPP, OOO and NNN;
- Short vector: the magnitude of short vectors is $U_{DC}/3$, including POO, PPO, OPO, OPP, OOP, POP, ONN, OON, NON, NOO, NOO, ONO;
- Medium vectors: the magnitude of medium vectors is $U_{DC}/\sqrt{3}$, including PON, OPN, NPO, NOP, ONP, PNO;
- Long vector: the magnitude of medium vectors is $2U_{DC}/3$, including PNN, PPN, NPN, NNP, NPP, NNP, PNP.

Untill now, we can use the three voltage level to deploy SVPWM strategy for the three-level inverter.

2.2 Three-level SVPWM strategy

The three-level SVPWM strategy is composed of sector choose, subsector choose, electrical vector choose, electrical vector dwell time calculation, and identification of switching sequence.

Let

$$V_a = V_m \sin(\omega t) \quad (2.1)$$

$$V_b = V_m \sin\left(\omega t - \frac{2\pi}{3}\right) \quad (2.2)$$

$$V_c = V_m \sin\left(\omega t + \frac{2\pi}{3}\right) \quad (2.3)$$

are the three-phase output voltage we need. Based on a balanced inverter operation, the three-phase voltage can be transformed to space vector coordinate by Clarke transform:

$$\begin{bmatrix} V_\alpha \\ V_\beta \end{bmatrix} = \frac{2}{3} \begin{bmatrix} 1 & -\frac{1}{2} & -\frac{1}{2} \\ 0 & \frac{\sqrt{3}}{2} & -\frac{\sqrt{3}}{2} \end{bmatrix} \begin{bmatrix} V_a \\ V_b \\ V_c \end{bmatrix} \quad (2.4)$$

The reference voltage vector in space vector coordinate can be expressed into $V_{ref} = V_\alpha + jV_\beta$, where the magnitude and phase of V_{ref} can be written into:

$$|V_{ref}| = \sqrt{V_\alpha^2 + V_\beta^2} \quad (2.5)$$

$$\theta = \tan^{-1} \frac{v_\beta(t)}{v_\alpha(t)} \quad (2.6)$$

After Clarke transform, we should locate the sector and subsector of V_{ref} in space vector coordinate, as shown in Fig. 2.7(a), which has six sectors and six subsectors. And there are total 27 vectors, 6 long vectors, 6 medium vectors, 12 short vectors and 3 zero vectors, as shown in Fig. 2.7(b).

Each sector has $\frac{\pi}{3}$ degree, as shown in Fig.2.8(a). The determination of sector is the same

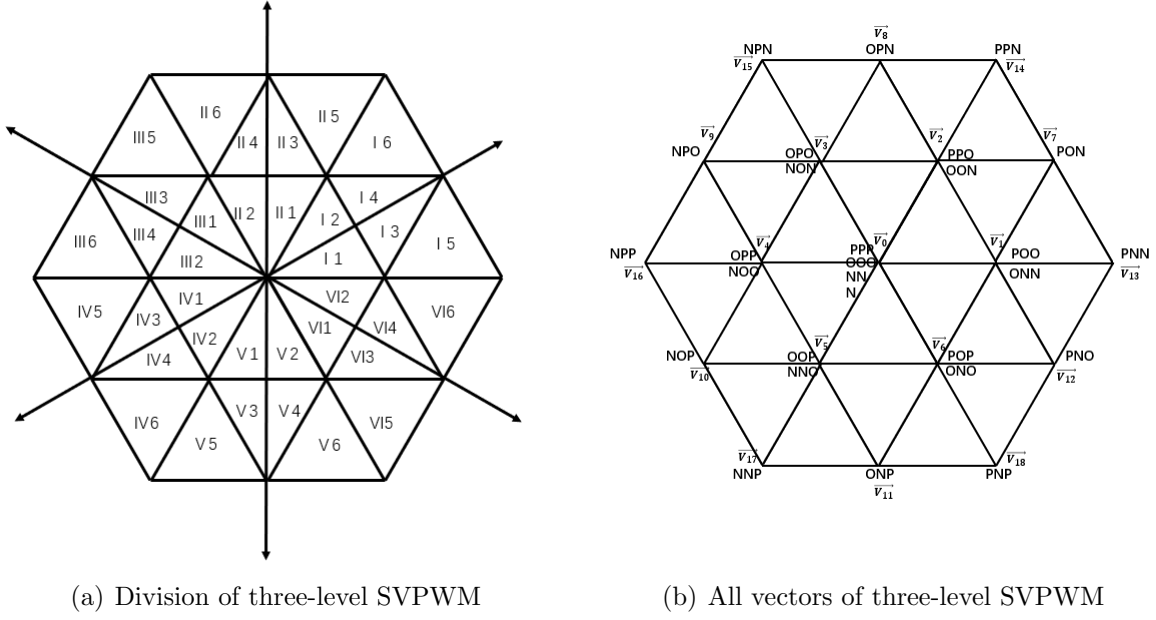


Figure 2.7: Vector distribution of three-level SVPWM

to two-level SVPWM, which can be determined by:

$$sector = \text{int}\left(\frac{\theta}{\pi/3}\right) + 1 \quad (2.7)$$

The division of subsector in sector I is shown in Fig. 2.8(b). First, we need to determine whether the voltage vector is in subsector 1, 3, 5 or 2, 4, 6. If $\theta < \frac{\pi}{6}$, we can have the vector is in subsector 1, 3, 5, else the vector would fall in subsector 2, 4, 6. We have known that the magnitude of α and β axis is $\frac{2}{3}V_{dc}$, therefore we can have:

- When $\theta < \frac{\pi}{6}$, and $V_\beta < -\sqrt{3}V_\alpha + \frac{\sqrt{3}}{3}V_{dc}$, V_{ref} falls in subsector 1.
- When $\theta < \frac{\pi}{6}$, and $V_\beta < \sqrt{3}V_\alpha - \frac{\sqrt{3}}{3}V_{dc}$, V_{ref} falls in subsector 5.
- When $\theta < \frac{\pi}{6}$, $V_\beta > -\sqrt{3}V_\alpha + \frac{\sqrt{3}}{3}V_{dc}$, $V_\beta > \sqrt{3}V_\alpha - \frac{\sqrt{3}}{3}V_{dc}$, V_{ref} falls in subsector 3.
- When $\theta > \frac{\pi}{6}$, and $V_\beta < -\sqrt{3}V_\alpha + \frac{\sqrt{3}}{3}V_{dc}$, V_{ref} falls in subsector 2.
- When $\theta > \frac{\pi}{6}$, and $V_\beta > \frac{\sqrt{3}}{6}V_{dc}$, V_{ref} falls in subsector 6.
- When $\theta > \frac{\pi}{6}$, $V_\beta > -\sqrt{3}V_\alpha + \frac{\sqrt{3}}{3}V_{dc}$ and $V_\beta < \frac{\sqrt{3}}{6}V_{dc}$, V_{ref} falls in subsector 4.

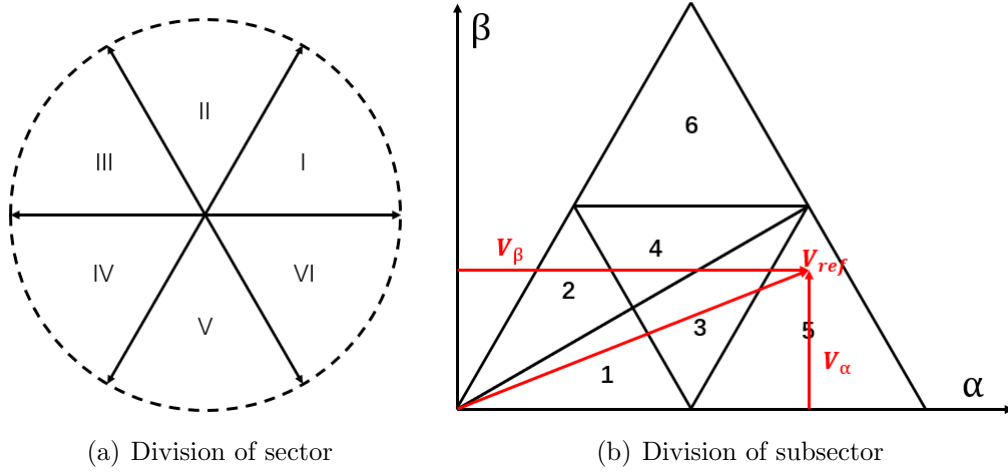


Figure 2.8: Determination of sector and subsector

The modulation index can also be utilized for subsector determination [11]. The length of the reference vector is resolved into two lengths m_1 and m_2 :

$$m_1 = m_n \left(\cos(\theta) - \frac{\sin(\theta)}{\sqrt{3}} \right) \quad (2.8)$$

$$m_2 = 2m_n \frac{\sin(\theta)}{\sqrt{3}} \quad (2.9)$$

$$m_n = \sqrt{m_a} \quad (2.10)$$

$$m_a = \text{modulation index} = \frac{\sqrt{3}V_{ref}}{V_{dc}} \quad (2.11)$$

- when $m_1 < 1$, $m_2 < 1$ and $m_1 + m_2 < 1$, V_{ref} falls in subsector 1 or 2.
- when $m_1 \leq 1$, $m_2 \leq 1$ and $m_1 + m_2 > 1$, V_{ref} falls in subsector 3 or 4.
- when $m_1 > 1$, V_{ref} falls in subsector 5.
- when $m_2 > 1$, V_{ref} falls in subsector 5.

The subsector determination of other sectors can be achieved by transforming the vector to sector I.

Based on the sector and subsector, we can determine each vector's electrical vector

combination and dwell time. Take sector I as an example. If V_{ref} falls in subsector 1 and 2, we need zero vector and two short vectors; if V_{ref} falls in subsector 3 and 4, we need two short vectors and one medium vector; if V_{ref} falls in subsector 5 and 6, we need one short vector, one medium vector, and one long vector. Detail vector combination is shown in Table. 2.2.

Table 2.2: Vector choose for each subsector in sector I

Subsector	V_1	V_2	V_3
1	V_1	V_2	V_0
2	V_1	V_2	V_0
3	V_1	V_2	V_7
4	V_1	V_2	V_7
5	V_1	V_7	V_{13}
6	V_2	V_7	V_{14}

Then according to voltage-second theory [12], we can have:

$$V_{ref\alpha} = T1 \times V_{1\alpha} + T2 \times V_{2\alpha} + T3 \times V_{3\alpha} \quad (2.12)$$

$$V_{ref\beta} = T1 \times V_{1\beta} + T2 \times V_{2\beta} + T3 \times V_{3\beta} \quad (2.13)$$

$$T_1 + T_2 + T_3 = T_s = 1/f_{sw} \quad (2.14)$$

where,

$$\begin{bmatrix} T_1 \\ T_2 \\ T_3 \end{bmatrix} = \begin{bmatrix} V_{1\alpha} & V_{1\alpha} & V_{1\alpha} \\ V_{1\beta} & V_{1\beta} & V_{1\beta} \\ 1 & 1 & 1 \end{bmatrix}^{-1} \begin{bmatrix} V_{ref\alpha} \\ V_{ref\beta} \\ 1/f_{sw} \end{bmatrix} \quad (2.15)$$

With the dwell time of each vector, we can generate PWM signals for each switch. The vector chosen for each subsector is shown in Table.2.4.

2.3 T-type inverter with SVPWM simulation

The proposed three-level T-type inverter is simulated in Simulink with the simulation parameters seen in Table. 2.3.

Table 2.3: Simulated three-level T-type inverter parameters

Parameter	Value	Parameter	Value
DC Bus Voltage	100VDC	V_{A1P-P}	25VAC
Line Frequency	60Hz	V_{A2P-P}	30VAC
Switching Frequency	10kHz	V_{A3P-P}	45VAC

The Simulink model is controlled in an open loop, which accepts three-phase voltage input. Based on the aforementioned subsector choose, we have the voltage vector will always fall on subsector 1 and 2 when phase voltage $V_A < \frac{\sqrt{3}}{6}V_{DC}$; the voltage vector will fall on subsector 1, 2, 3 and 4 when $\frac{\sqrt{3}}{6}V_{DC} < V_A < \frac{1}{3}V_{DC}$; the voltage vector will fall on subsector 3, 4, 5 and 6 when $\frac{1}{3}V_{DC} < V_A$, and V_{DC} should always be lower than $\frac{\sqrt{3}}{3}V_{DC}$. Therefore, three voltage magnitudes are chosen to have the voltage vector meet the requirements of different subsector choose conditions.

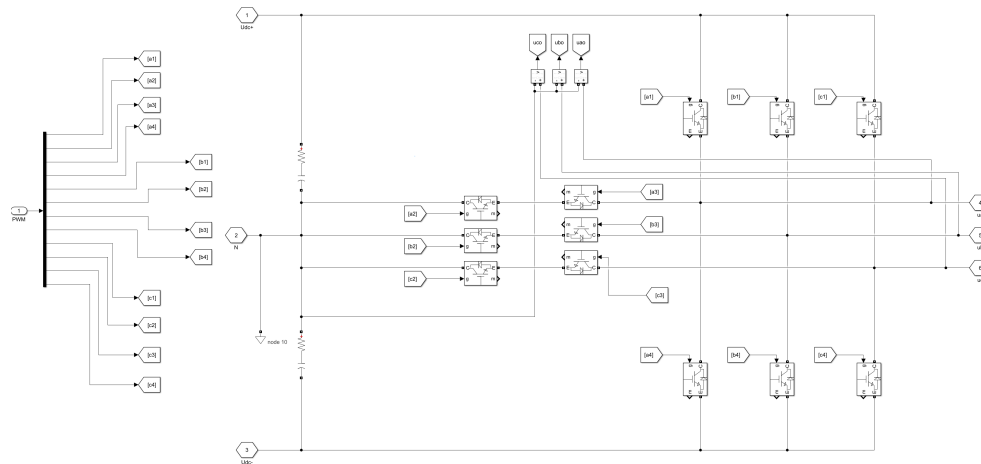


Figure 2.9: Three-level T-type inverter simulation

The circuit model is shown in Fig. 2.9. Manufacturer-supplied switch models with adjustable $R_{ds(on)}$ and dead time were used to model to simulate realistic conditions.

When $V_{a_{peak}} = 25V$, the voltage vector always falls on subsectors 1 and 2. The sector, subsector, vector dwelling time, phase voltage, line voltage and line voltage FFT analysis is also shown in Fig. 2.10.

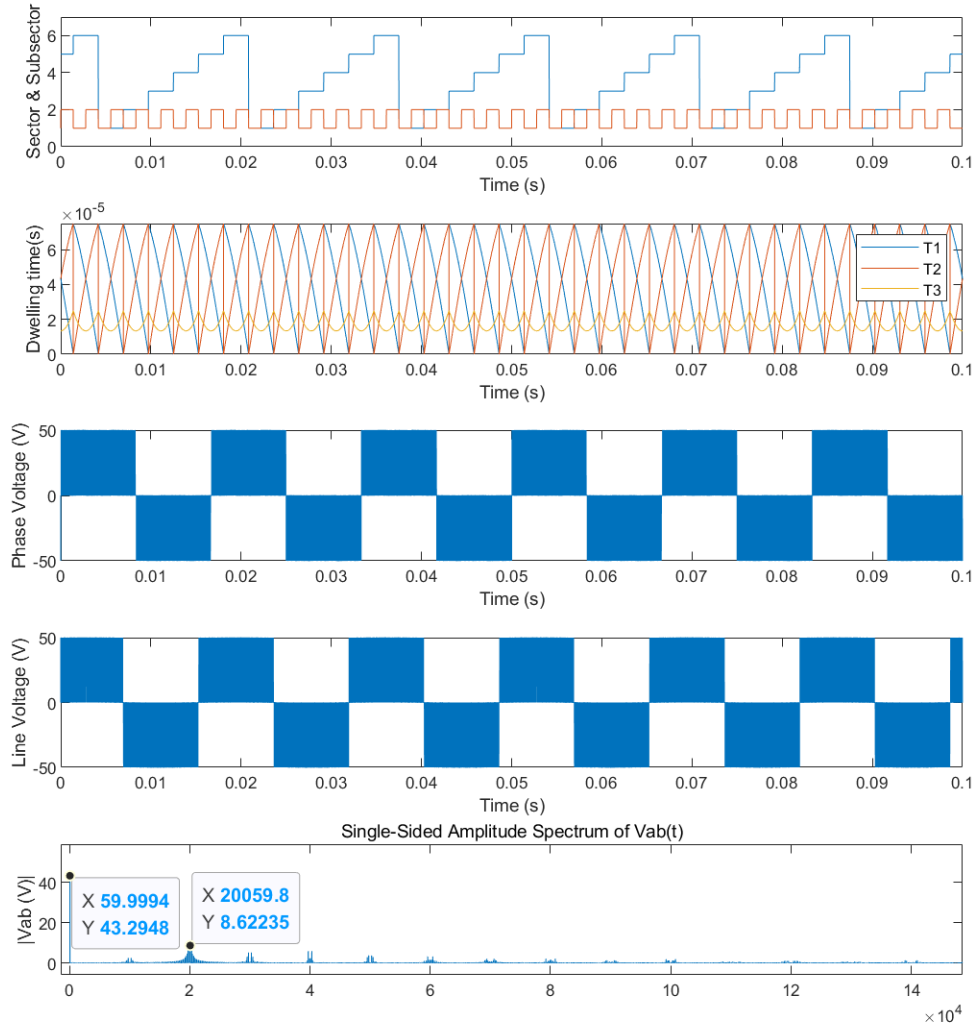


Figure 2.10: Sector, subsector, vector dwelling time, phase voltage, line voltage and line voltage FFT analysis when $V_a = 25V$

When $V_{a_{peak}} = 30V$, the voltage vector always falls on subsectors 1, 2 3, and 4. The sector, subsector, vector dwelling time, and voltage are shown in Fig. 2.11. When $V_{a_{peak}} = 30V$, $V_{ab_{peak}} = 30\sqrt{3}V$, while frequency is 60Hz. The FFT analysis is also shown in Fig. 2.11.

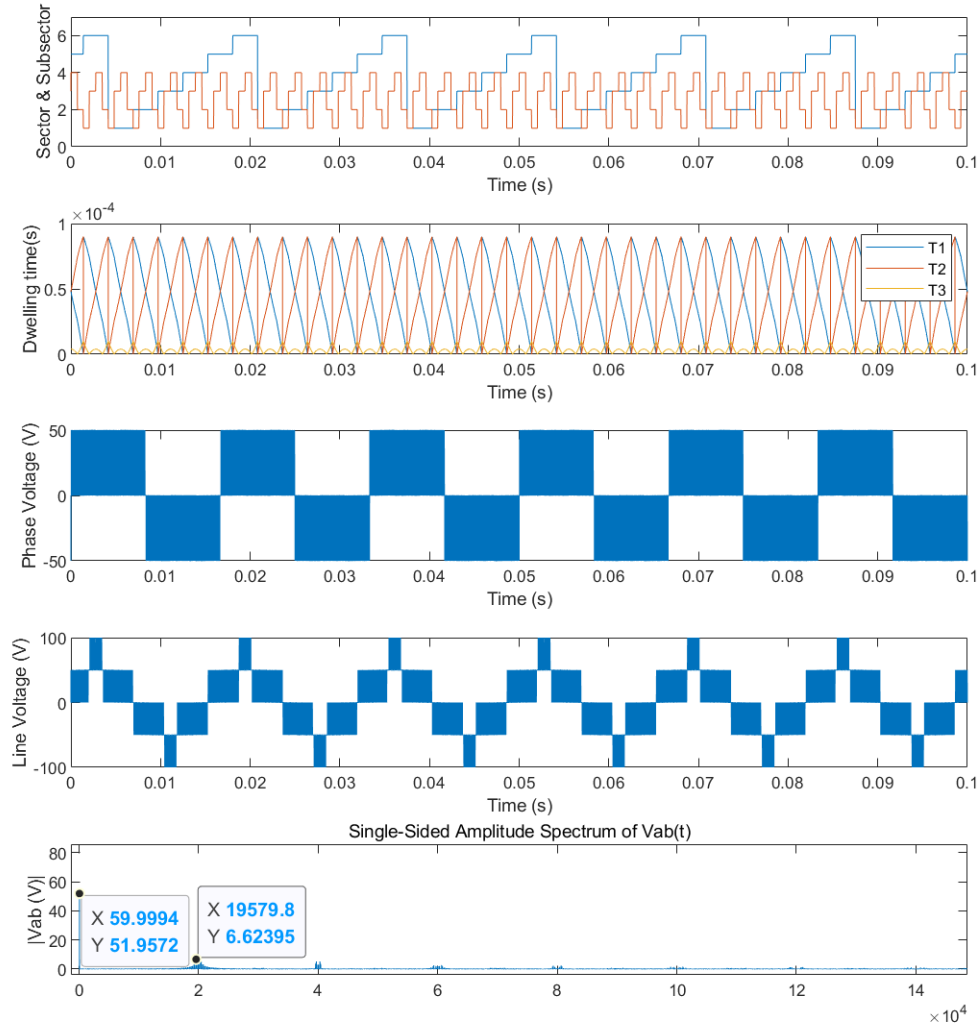


Figure 2.11: Sector, subsector, vector dwelling time, phase voltage, line voltage and line voltage FFT analysis when $V_a = 30V$

When $V_{a_{peak}} = 45V$, the voltage vector always falls on subsector 3, 4 5, and 6. The sector, subsector, vector dwelling time, and voltage are shown in Fig. 2.12. When $V_{a_{peak}} = 45V$, $V_{ab_{peak}} = 45\sqrt{3}V$, while frequency is 60Hz. The FFT analysis is shown in Fig. 2.12.

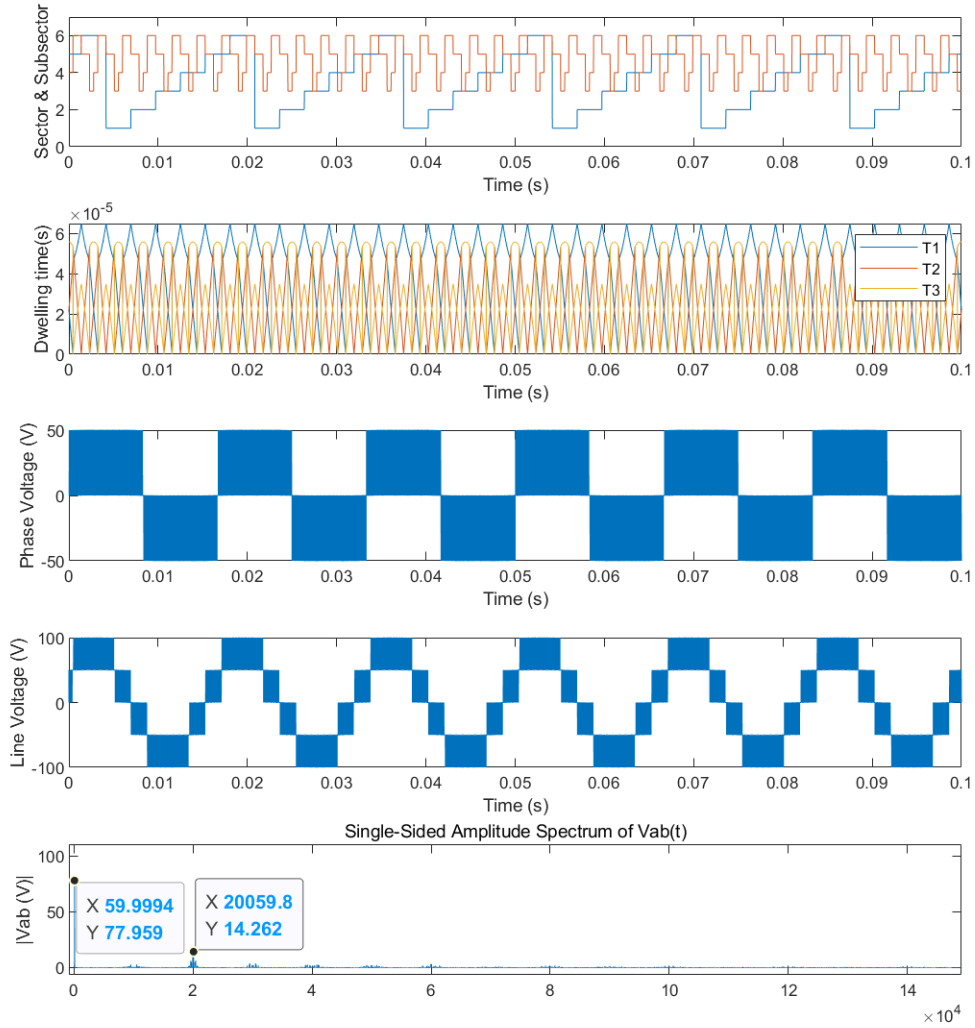


Figure 2.12: Sector, subsector, vector dwelling time, phase voltage, line voltage and line voltage FFT analysis when $V_a = 45V$

2.4 Filter Design

This three-level inverter is designed for sensorless motor control, while the sensorless control algorithm is based on a back EMF observer, which requires an accurate sinusoidal voltage sampling [13]. However, the voltage sensor at the output terminal can only read the PWM voltage output (five voltage level) instead of a sinusoidal voltage, as shown in Fig. 2.13.

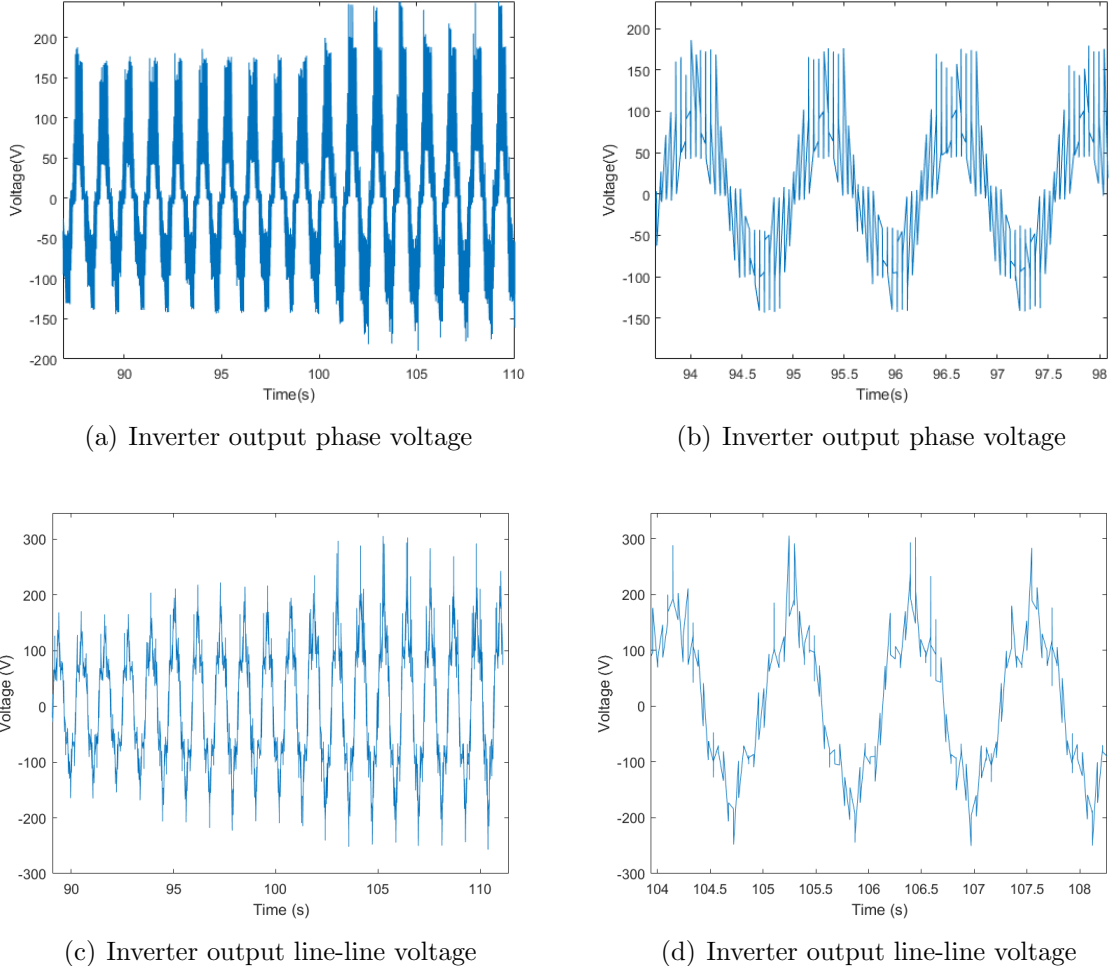


Figure 2.13: Output voltage sampling without filter

The unfiltered voltage injects too much harmonics and noise, though does not influence the motor, but leads to a huge error on the rotor position estimation. Therefore, a filter is needed. Based on the literature, a high-order LCL filter can provide efficient harmonic attenuation [14], as shown in Fig. 2.14.

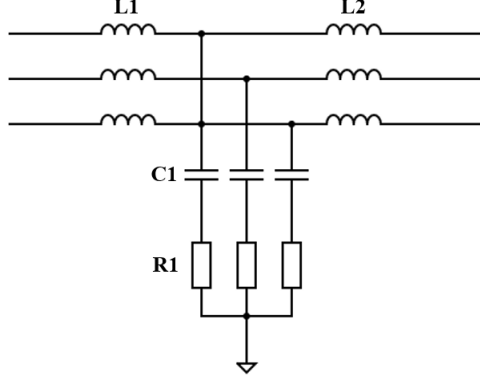


Figure 2.14: A high-order LCL filter

The first inductor L_1 can be derived from [15]:

$$L_1 = \frac{V_{DC}}{8 \times f_{sw} \times I_{rated} \times \%ripple} = \frac{100V}{8 \times 10kHz \times 8A \times 5\%} = 312\mu H \quad (2.16)$$

Similarly, the value of the capacitor C_1 can be determined by [15]:

$$C_1 = \frac{\%X \times P_{rated}}{2 \times \pi \times f_{motor} \times V_{rated}^2} = \frac{5\% \times 1kW}{2 \times \pi \times 60Hz \times (100V)^2} = 13.263\mu F \quad (2.17)$$

where $\%x$ is the total reactive power absorbed by the capacitor.

Furthermore, to have 50% attenuation factor, the second inductor can be derived from [15]:

$$L_2 = \left| \frac{\frac{1}{50\%} - 1}{1 - L_1 \times \frac{C_1}{x\%} \times (2 \times f_{sw})^2 \times x\%} \right| \times L_1 \quad (2.18)$$

$$= \left| \frac{\frac{1}{50\%} - 1}{1 - 312\mu H \times 13.26\mu F \times (2 \times 10kHz)^2} \right| \times L_1 = 20\mu H \quad (2.19)$$

The resonance frequency and damping resistor of this LCL filter can be derived from [14]:

$$f_{res} = \frac{1}{2 \sqrt{\frac{L_1 \times L_2}{L_1 + L_2} \times C_1}} = \frac{1}{2 \sqrt{\frac{20\mu H \times 312\mu H}{20\mu H + 312\mu H} \times 13.26\mu F}} = 10kHz \quad (2.20)$$

$$R_1 = \frac{1}{6 \times \pi \times f_{res} \times C_1} = \frac{1}{6 \times \pi \times 10kHz \times 13.26\mu F} = 0.39\Omega \quad (2.21)$$

With the filter, the PWM voltage can be filtered to a significant sinusoidal voltage, which is suitable for being sensed by the voltage sensor and can be employed to estimate back EMF. This LCL filter is simulated in Simulink with the aforementioned T-type inverter to verify the filtering performance. The peak voltage of phase voltage is set to 45V. The Phase voltage, line voltage, and FFT analysis of line voltage are shown in Fig. 2.15.

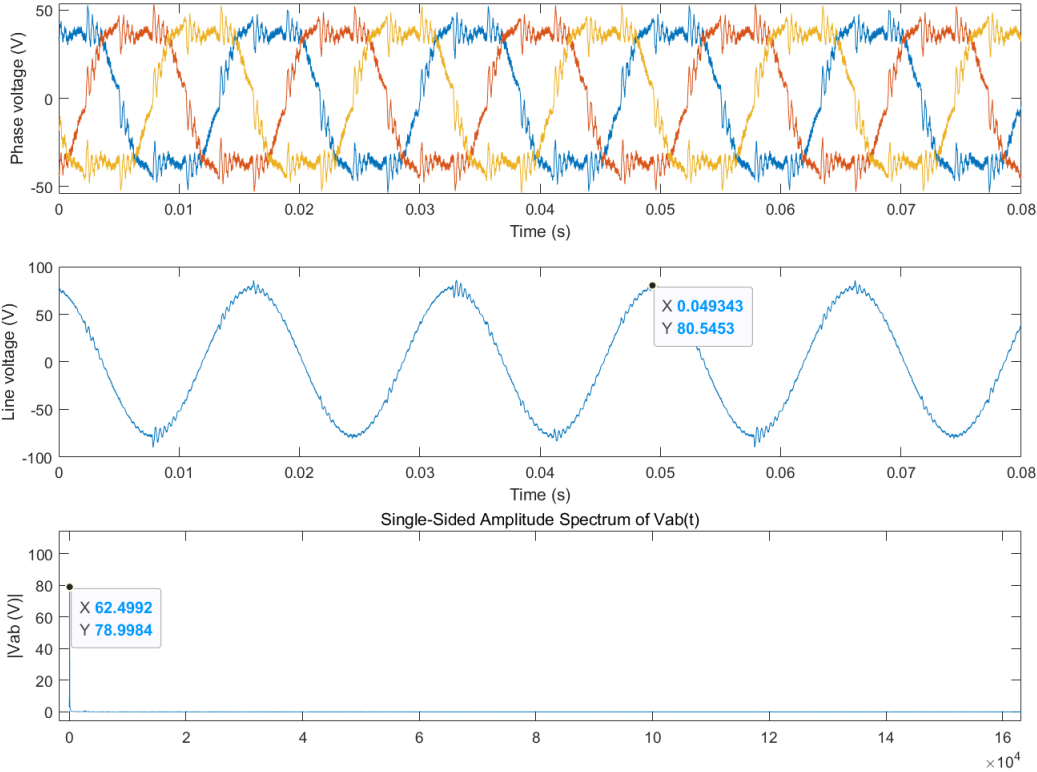
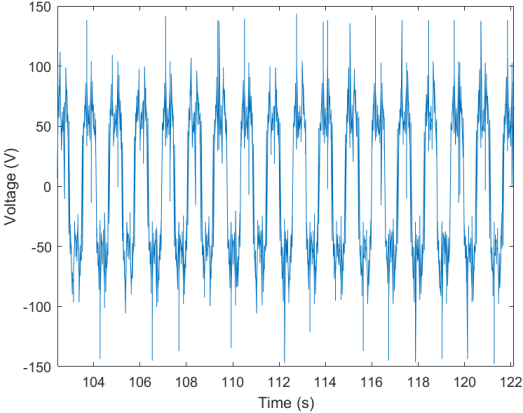


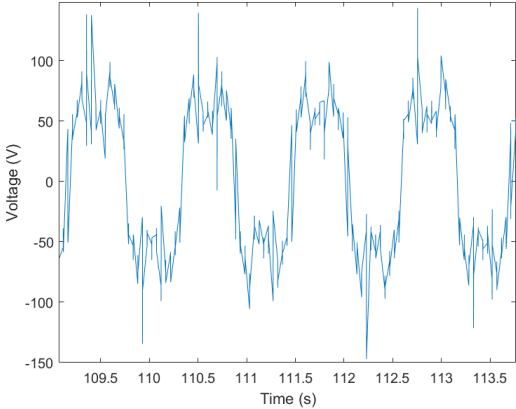
Figure 2.15: Simulated phase, line voltage, and FFT analysis of filtered T-type inverter

The phase voltage is analogous to a sinusoidal voltage with a third harmonic injection, demonstrating the successful achievement of space vector PWM. The third harmonic injection can increase the DC bus voltage utilization significantly [16]. The line-line voltage is sinusoidal as expected, while the FFT analysis presents the main component as a 60Hz voltage with 78V magnitude. Compared with the unfiltered waveform shown in Fig. 2.12, some higher-order harmonics are also filtered.

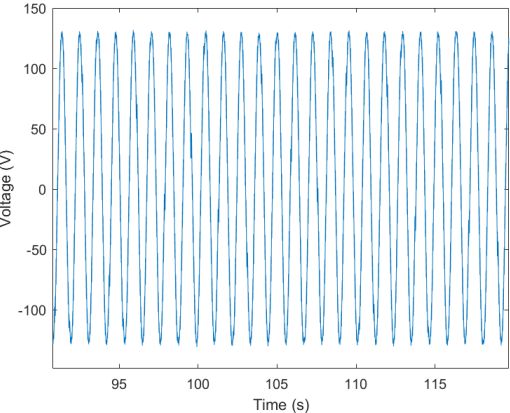
The phase voltage and line-line voltage sampled by the voltage sensor are shown in Fig. 2.16. The phase voltage and line-line voltage both match the simulation.



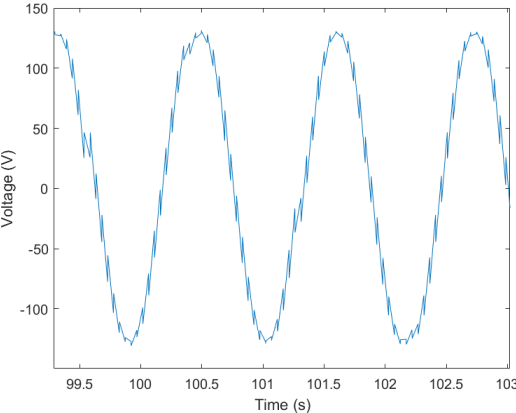
(a) Inverter output phase voltage



(b) Inverter output phase voltage



(c) Inverter output line-line voltage



(d) Inverter output line-line voltage

Figure 2.16: Output voltage sampling with filter

Table 2.4: Vector Sequence and dwelling time

Region	Vector sequence							Vector index		
	$\frac{T_1}{4}$	$\frac{T_2}{2}$	$\frac{T_3}{2}$	$\frac{T_1}{2}$	$\frac{T_3}{2}$	$\frac{T_2}{2}$	$\frac{T_1}{4}$	T_1	T_2	T_3
I1	ONN	OON	OOO	POO	OOO	OON	ONN	V_1	V_2	V_0
I2	OON	OOO	POO	PPO	POO	OOO	OON	V_2	V_0	V_1
I3	ONN	OON	PON	POO	PON	OON	ONN	V_1	V_2	V_7
I4	OON	PON	POO	PPO	POO	PON	OON	V_2	V_7	V_1
I5	ONN	PNN	PON	POO	PON	PNN	ONN	V_1	V_{13}	V_7
I6	OON	PON	PPN	PPO	PPN	PON	OON	V_2	V_7	V_{14}
II1	OON	OOO	OPO	PPO	OPO	OOO	OON	V_2	V_0	V_3
II2	NON	OON	OOO	OPO	OOO	OON	NON	V_3	V_2	V_0
II3	OON	OPN	OPO	PPO	OPO	OPN	OON	V_2	V_8	V_3
II4	NON	OON	OPN	OPO	OPN	OON	NON	V_3	V_2	V_8
II5	OON	OPN	PPN	PPO	PPN	OPN	OON	V_2	V_8	V_{14}
II6	NON	NPN	OPN	OPO	OPN	NPN	NON	V_3	V_{15}	V_8
III1	NON	NOO	OOO	OPO	OOO	NOO	NON	V_3	V_4	V_0
III2	NOO	OOO	OPO	OPP	OPO	OOO	NOO	V_4	V_0	V_3
III3	NON	NOO	NPO	OPO	NPO	NOO	NON	V_3	V_4	V_9
III4	NOO	NPO	OPO	OPP	OPO	NPO	NOO	V_4	V_9	V_3
III5	NON	NPN	NPO	OPO	NPO	NPN	NON	V_3	V_{15}	V_9
III6	NOO	NPO	NPP	OPP	NPP	NPO	NOO	V_4	V_9	V_{16}
IV1	NOO	OOO	OOP	OPP	OOP	OOO	NOO	V_4	V_0	V_5
IV2	NNO	NOO	OOO	OOP	OOO	NOO	NNO	V_5	V_4	V_0
IV3	NOO	NOP	OOP	OPP	OOP	NOP	NOO	V_4	V_{10}	V_5
IV4	NNO	NOO	NOP	OOP	NOP	NOO	NNO	V_5	V_4	V_{10}
IV5	NOO	NOP	NPP	OPP	NPP	NOP	NOO	V_4	V_{10}	V_{16}
IV6	NNO	NNP	NOP	OOP	NOP	NNP	NNO	V_5	V_{17}	V_{10}
V1	NNO	ONO	OOO	OOP	OOO	ONO	NNO	V_5	V_6	V_0
V2	ONO	OOO	OOP	POP	OOP	OOO	ONO	V_6	V_0	V_5
V3	NNO	ONO	ONP	OOP	ONP	ONO	NNO	V_5	V_6	V_{11}
V4	ONO	ONP	OOP	POP	OOP	ONP	ONO	V_6	V_{11}	V_5
V5	NNO	NNP	ONP	OOP	ONP	NNP	NNO	V_5	V_{17}	V_{11}
V6	ONO	ONP	PNP	POP	PNP	ONP	ONO	V_6	V_{11}	V_{18}
VI1	ONO	OOO	POO	POP	POO	OOO	ONO	V_6	V_0	V_1
VI2	ONN	ONO	OOO	POO	OOO	ONO	ONN	V_1	V_6	V_0
VI3	ONO	PNO	POO	POP	POO	PNO	ONO	V_6	V_{12}	V_1
VI4	ONN	ONO	PNO	POO	PNO	ONO	ONN	V_1	V_6	V_{12}
VI5	ONO	PNO	PNP	POP	PNP	PNO	ONO	V_6	V_{12}	V_{18}
VI6	ONN	PNN	PNO	POO	PNO	PNN	ONN	V_1	V_{13}	V_{12}

Chapter 3

Sensorless Control of an IPMSM

IPMSM stands for Interior Permanent Magnet Synchronous Motor, which is a type of electric motor used in various applications such as electric vehicles, industrial automation, and renewable energy systems.

One advantage of IPMSM is its high efficiency due to the permanent magnets installed in the rotor, which generate a magnetic field that interacts with the stator's magnetic field, resulting in a high torque density and power output. The IPMSM also has a high power factor, which means that it can deliver more power while consuming less energy.

Additionally, IPMSMs offer high reliability and durability due to their simple structure, which makes them less prone to wear and tear. They also have a high power-to-weight ratio, making them suitable for applications where space and weight are a concern.

Sensorless control for IPMSM is a method of controlling the motor without the need for external sensors such as encoders or hall effect sensors, instead using an observer and some signal processing techniques to estimate the motor's position and speed. One reason why sensorless control for IPMSM is necessary is that external sensors can be expensive and may add complexity to the motor control system. By eliminating the need for external sensors, the cost of the motor control system can be reduced, and the overall system design can be simplified.

Another reason for using sensorless control is that external sensors can be prone to wear and tear and can be affected by harsh operating environments. By using sensorless control, maintenance costs can also be reduced.

This section will present how sensorless control is achieved with two different observers, including a back EMF sliding mode observer [3] and a flux linkage nonlinear observer [17], and compare the performance between these two techniques.

3.1 IPMSM dynamic model

This section presents the dynamic model for an IPMSM under ABC , and dq references. The speed controller and current controller design are also presented.

The stator voltage equations of IPMSM are expressed as:

$$\begin{bmatrix} u_a \\ u_b \\ u_c \end{bmatrix} = \begin{bmatrix} R_a & 0 & 0 \\ 0 & R_b & 0 \\ 0 & 0 & R_c \end{bmatrix} \begin{bmatrix} i_a \\ i_b \\ i_c \end{bmatrix} + \frac{d}{dt} \begin{bmatrix} \lambda_a \\ \lambda_b \\ \lambda_c \end{bmatrix} \quad (3.1)$$

The flux linkages for stator winding can be written as:

$$\begin{bmatrix} \lambda_a \\ \lambda_b \\ \lambda_c \end{bmatrix} = L_{abc} \begin{bmatrix} L_{aa} & L_{ab} & L_{ac} \\ L_{ab} & L_{bb} & L_{bc} \\ L_{ac} & L_{bc} & L_{cc} \end{bmatrix} \begin{bmatrix} i_a \\ i_b \\ i_c \end{bmatrix} + \begin{bmatrix} \lambda_{pm} \cos(\theta) \\ \lambda_{pm} \cos(\theta - \frac{2}{3}\pi) \\ \lambda_{pm} \cos(\theta + \frac{2}{3}\pi) \end{bmatrix} \quad (3.2)$$

The next step is to convert the three-phase equations into dq reference frame with Clarke and Park transformation:

$$\begin{aligned} u_d &= R_s i_d + \frac{d\lambda_d}{dt} - \omega_e \lambda_q \\ u_q &= R_s i_q + \frac{d\lambda_q}{dt} - \omega_e \lambda_d \end{aligned} \quad (3.3)$$

where i_d and i_q are d axis and q axis stator current, R_s is the stator resistance and ω_e is

the electrical speed of the motor. The stator flux components λ_d and λ_q are:

$$\lambda_d = L_d i_d + \lambda_r; \quad \lambda_q = L_q i_q \quad (3.4)$$

where L_d and L_q are d axis and q axis inductance, and λ_r is the permanent magnet flux. The torque is given by:

$$\tau_e = \frac{3}{2} p i_q [\lambda_r + (L_d - L_q) i_d] \quad (3.5)$$

where p is the pole pairs. The mechanical rotor speed is calculated using

$$\tau_e - \tau_L = B \omega_m + J \frac{d\omega_m}{dt} \quad (3.6)$$

where

- τ_e : Electromagnetic torque produced by the machine
- τ_L : Load torque
- B : Damping coefficient
- J : Machine inertia constant
- ω_m : Rotor mechanical speed

The product of mechanical speed and pole pairs is the electrical speed, and we can have

$$\omega_e = \omega_m \times p \quad (3.7)$$

$$\tau_e - \tau_L = p B \omega_e + p J \frac{d\omega_e}{dt} \quad (3.8)$$

Based on the dynamic model, an IPMSM is simulated in Simulink, with the motor parameters shown in Table. 3.1.

Table 3.1: Simulation IPMSM parameters

Parameter	Value
λ_r	0.1034wb
p	4
L_d	0.845mH
L_q	2.217mH
R_s	0.0592Ω
J	0.12kgm ²
B	$8.09 \times 10^{-4}Ns/m$

3.2 IPMSM back-EMF SMO observer

The critical point for sensorless control is to know the speed and angle of the rotor, and with the position information, Park transformation can be utilized to transfer rotating components to a DC value, which we can use the speed controller and current controller to control.

Apply inverse Park transformation to Eq. 3.3, we can have:

$$u(i)_\alpha = u(i)_d \cos(\theta_e) - u(i)_q \sin(\theta_e) \quad (3.9)$$

$$u(i)_\beta = u(i)_d \sin(\theta_e) + u(i)_q \cos(\theta_e)$$

Where θ_e is the electrical angle. Rewrite the IPMSM model in $\alpha\beta$ reference:

$$\begin{bmatrix} u_\alpha \\ u_\beta \end{bmatrix} = R_s \begin{bmatrix} i_\alpha \\ i_\beta \end{bmatrix} + \begin{bmatrix} L_\alpha & L_{\alpha\beta} \\ L_{\alpha\beta} & L_\alpha \end{bmatrix} \frac{d}{dt} \begin{bmatrix} i_\alpha \\ i_\beta \end{bmatrix} + \begin{bmatrix} -\lambda_r \omega_e \sin(\theta_e) \\ \lambda_r \omega_e \cos(\theta_e) \end{bmatrix} \quad (3.10)$$

where

$$L_1 = (L_d + L_q)/2; \quad L_2 = (L_d - L_q)/2$$

$$L_\alpha = L_1 + L_2 \cos(2\theta_e); \quad L_\beta = L_1 - L_2 \cos(2\theta_e); \quad L_{\alpha\beta} = L_2 \sin(2\theta_e)$$

and Eq. 3.10 can be written into [18]:

$$\begin{aligned} \begin{bmatrix} u_\alpha \\ u_\beta \end{bmatrix} &= R_s \begin{bmatrix} i_\alpha \\ i_\beta \end{bmatrix} + \begin{bmatrix} L_d & 0 \\ 0 & L_d \end{bmatrix} \frac{d}{dt} \begin{bmatrix} i_\alpha \\ i_\beta \end{bmatrix} + \begin{bmatrix} 0 & \omega_e(L_d - L_q) \\ \omega_e(L_q - L_d) & 0 \end{bmatrix} \begin{bmatrix} i_\alpha \\ i_\beta \end{bmatrix} \\ &+ [(L_d - L_q)(\omega_e i_d - \frac{d}{dt} i_q) + \lambda_r \omega_e] \begin{bmatrix} -\sin(\theta_e) \\ \cos(\theta_e) \end{bmatrix} \end{aligned} \quad (3.11)$$

In Eq. 3.11, we can observe that the last item includes the position information we need θ_e , which is the back EMF of the IPMSM:

$$\begin{bmatrix} E_\alpha \\ E_\beta \end{bmatrix} = [(L_d - L_q)(\omega_e i_d - \frac{d}{dt} i_q) + \lambda_r \omega_e] \begin{bmatrix} -\sin(\theta_e) \\ \cos(\theta_e) \end{bmatrix} \quad (3.12)$$

Take Eq. 3.12 back into Eq. 3.11, we can have:

$$\begin{bmatrix} u_\alpha \\ u_\beta \end{bmatrix} = \begin{bmatrix} L_d & 0 \\ 0 & L_d \end{bmatrix} \frac{d}{dt} \begin{bmatrix} i_\alpha \\ i_\beta \end{bmatrix} + \begin{bmatrix} R_s & \omega_e(L_d - L_q) \\ \omega_e(L_q - L_d) & R_s \end{bmatrix} \begin{bmatrix} i_\alpha \\ i_\beta \end{bmatrix} + \begin{bmatrix} E_\alpha \\ E_\beta \end{bmatrix} \quad (3.13)$$

Rewrite Eq. 3.13 into:

$$\frac{d}{dt} \begin{bmatrix} i_\alpha \\ i_\beta \end{bmatrix} = \frac{1}{L_d} \begin{bmatrix} -R_s & \omega_e(L_q - L_d) \\ \omega_e(L_d - L_q) & -R_s \end{bmatrix} \begin{bmatrix} i_\alpha \\ i_\beta \end{bmatrix} + \frac{1}{L_d} \begin{bmatrix} u_\alpha \\ u_\beta \end{bmatrix} - \frac{1}{L_d} \begin{bmatrix} E_\alpha \\ E_\beta \end{bmatrix} \quad (3.14)$$

To compute the E_α and E_β , the sliding mode observer is designed into:

$$\frac{d}{dt} \begin{bmatrix} \hat{i}_\alpha \\ \hat{i}_\beta \end{bmatrix} = \frac{1}{L_d} \begin{bmatrix} -R_s & \omega_e(L_q - L_d) \\ \omega_e(L_d - L_q) & -R_s \end{bmatrix} \begin{bmatrix} \hat{i}_\alpha \\ \hat{i}_\beta \end{bmatrix} + \frac{1}{L_d} \begin{bmatrix} u_\alpha \\ u_\beta \end{bmatrix} - \frac{1}{L_d} \begin{bmatrix} v_\alpha \\ v_\beta \end{bmatrix} \quad (3.15)$$

\hat{i}_α and \hat{i}_β are estimated $\alpha\beta$ current, and v_α and v_β are controlled input of the observer, which

can be expressed into:

$$\begin{bmatrix} v_\alpha \\ v_\beta \end{bmatrix} = \begin{bmatrix} h \cdot \text{sign}(\hat{i}_\alpha - i_\alpha) \\ h \cdot \text{sign}(\hat{i}_\beta - i_\beta) \end{bmatrix} \quad (3.16)$$

Make $\tilde{i}_\alpha = \hat{i}_\alpha - i_\alpha$, and $\tilde{i}_\beta = \hat{i}_\beta - i_\beta$, which stand for the error of estimated current from the real current. Use Eq. 3.15 subtract Eq. 3.14, we can have:

$$\frac{d}{dt} \begin{bmatrix} \tilde{i}_\alpha \\ \tilde{i}_\beta \end{bmatrix} = \frac{1}{L_d} \begin{bmatrix} -R_s & \omega_e(L_q - L_d) \\ \omega_e(L_d - L_q) & -R_s \end{bmatrix} \begin{bmatrix} \tilde{i}_\alpha \\ \tilde{i}_\beta \end{bmatrix} + \frac{1}{L_d} \begin{bmatrix} E_\alpha - v_\alpha \\ E_\beta - v_\beta \end{bmatrix} \quad (3.17)$$

When the estimated current is larger than the real current, there would be a positive input $v_{\alpha\beta}$. h is the observer gain, and the observer gain determines whether $\hat{i}_{\alpha\beta}$ can or not converge to $i_{\alpha\beta}$ and how fast is the convergence. If the gain is too small, it can not converge; if the gain is too high, the current will fluctuate significantly, which introduces extra error.

According to Lyapunov stability theorem [19], for a independent variable s_1 and a system $\dot{s}_1 = f(s_1)$, if there is a function $U(s_1)$ makes Eq. 3.18 valid, then $U(s_1)$ is a Lyapunov candidate function and the system $\dot{s}_1 = s_1$ is global asymptotic stability to $s_1 = 0$.

$$U(s_1) \leq 0 \quad \text{and} \quad \dot{U}(s_1) < 0 \quad \text{for} \quad s_1 \neq 0 \quad (3.18)$$

Therefore, we can construct a function:

$$U(\tilde{i}_\alpha) = \frac{\tilde{i}_\alpha \cdot \tilde{i}_\alpha}{2} \quad (3.19)$$

Thus, the derivative of this function is:

$$\dot{U}(\tilde{i}_\alpha) = \tilde{i}_\alpha \cdot \frac{d}{dt} \tilde{i}_\alpha \quad (3.20)$$

According to Eq. 3.15, we can rewrite Eq. 3.20, and we should have Eq. 3.20 < 0:

$$\tilde{i}_\alpha \cdot \frac{d\tilde{i}_\alpha}{dt} = \tilde{i}_\alpha \left[-\frac{R_s}{L_d} \tilde{i}_\alpha + \frac{\omega_e(L_q - L_d)}{L_d} \tilde{i}_\beta + \frac{1}{L_d} E_\alpha - \frac{1}{L_d} h \cdot \text{sign}(\tilde{i}_\alpha) \right] < 0 \quad (3.21)$$

Therefore, we can have the observer gain should satisfy the following equation:

$$h > -R_s |\tilde{i}_\alpha| + E_\alpha \cdot \text{sign}(\tilde{i}_\alpha) + \omega_e(L_q - L_d) \tilde{i}_\beta \cdot \text{sign}(\tilde{i}_\alpha) \quad (3.22)$$

Similarly, the observer gain should also satisfy the \tilde{i}_β requirement, which is:

$$h > -R_s |\tilde{i}_\beta| + E_\beta \cdot \text{sign}(\tilde{i}_\beta) + \omega_e(L_q - L_d) \tilde{i}_\alpha \cdot \text{sign}(\tilde{i}_\beta) \quad (3.23)$$

When the observer gain h satisfies all aforementioned requirements, \tilde{i}_α and \tilde{i}_β will converge to 0, which means the error of estimated current is 0. Therefore, Eq. 3.17 can be simplified into:

$$\begin{bmatrix} E_\alpha - v_\alpha \\ E_\beta - v_\beta \end{bmatrix} = \begin{bmatrix} 0 \\ 0 \end{bmatrix} \quad (3.24)$$

Therefore, we can have:

$$\begin{bmatrix} E_\alpha \\ E_\beta \end{bmatrix} = \begin{bmatrix} h \cdot \text{sign}(\hat{i}_\alpha - i_\alpha) \\ h \cdot \text{sign}(\hat{i}_\beta - i_\beta) \end{bmatrix} \quad (3.25)$$

Furthermore, we have previously discussed that the observer control input in Eq. 3.16 contains a *sign* function of the current observation error. Even if the current error is only tiny, the control input will still give a signal with an amplitude of h , which can cause excessive fluctuation. To suppress excessive fluctuation, we can use a *saturation* function (shown in Eq. 3.26) instead of the *sign* function without influencing the stability, and the magnitude of

control input can change with the magnitude of current error $\tilde{i}_{\alpha\beta}$.

$$\begin{bmatrix} E_\alpha \\ E_\beta \end{bmatrix} = \begin{bmatrix} h \cdot \text{sat}(\hat{i}_\alpha - i_\alpha) \\ h \cdot \text{sat}(\hat{i}_\beta - i_\beta) \end{bmatrix} \quad \text{sat}(x) = \begin{cases} x & -1 \leq x \leq 1 \\ 1 \text{ or } -1 & \text{when } x > 1 \text{ or } x < -1 \end{cases} \quad (3.26)$$

$\begin{bmatrix} E_\alpha \\ E_\beta \end{bmatrix}$ includes the rotor position θ_e , and a phase lock loop can be utilized to extract θ_e [18]. Similarly, we make $\hat{\theta}_e$ as the estimated angle of the rotor and $\tilde{\theta}_e = \theta_e - \hat{\theta}_e$ as the error of the estimated angle. When $\theta_e \approx 0$, we have $\sin(\theta_e) = \theta_e$. Therefore, we can have:

$$\sin(\theta_e)\cos(\hat{\theta}_e) - \cos(\theta_e)\sin(\hat{\theta}_e) = \sin(\theta_e - \hat{\theta}_e) = \sin(\tilde{\theta}_e) = \tilde{\theta}_e \quad (3.27)$$

Combine Eq. 3.27 and Eq. 3.12, and replace $[(L_d - L_q)(\omega_e i_d - \frac{d}{dt}i_q) + \lambda_r \omega_e]$ with k_2 we can have:

$$\begin{aligned} & -E_\alpha \cos(\hat{\theta}_e) - E_\beta \sin(\hat{\theta}_e) \\ & = [(L_d - L_q)(\omega_e i_d - \frac{d}{dt}i_q) + \lambda_r \omega_e] [\sin(\theta_e)\cos(\hat{\theta}_e) - \cos(\theta_e)\sin(\hat{\theta}_e)] = k_2 \tilde{\theta}_e \end{aligned} \quad (3.28)$$

Feed $k_2 \tilde{\theta}_e$ into a PI controller, we can know the estimated electrical speed $\hat{\omega}_e$, and after an integrator, we can have the estimated electrical angle $\hat{\theta}_e$, as shown in Fig. 3.1

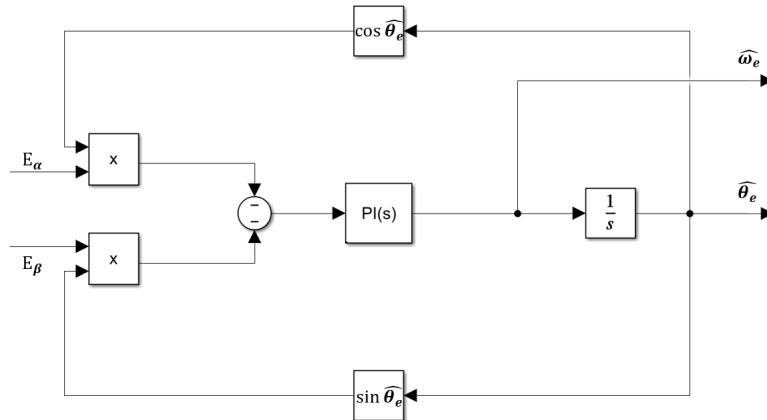


Figure 3.1: Phase lock loop

Therefore, we can have:

$$k_2(\theta_e - \hat{\theta}_e)(K_p + \frac{K_i}{s})\frac{1}{s} = \hat{\theta}_e \quad (3.29)$$

The transfer function of θ_e and $\hat{\theta}_e$ is:

$$\frac{\hat{\theta}_e}{\theta_e} = \frac{k_2K_p s + k_2K_i}{s^2 + k_2K_p s + k_2K_i} \quad (3.30)$$

The gain of the PI controller can be computed by:

$$K_i = \frac{\omega_n^2}{k_2} \quad K_p = \frac{2\omega_n}{k_2} \quad (3.31)$$

where ω_n is higher than the fundamental frequency of the IPMSM.

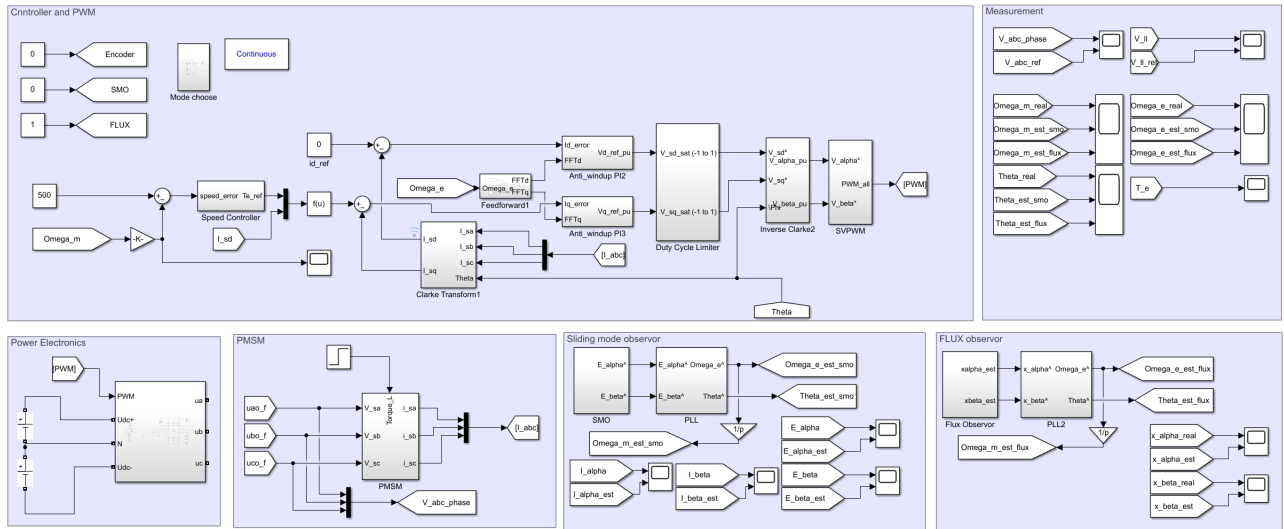


Figure 3.2: Simulink model diagram of sensorless control IPMSM

3.3 SMO sensorless control simulation

To test the performance of SMO-based sensorless control, an IPMSM model with speed& current controllers, three-level SVPWM strategy, and T-type inverter is simulated in Simulink, as shown in Fig. 3.2.

First, the IPMSM is driven by real position and speed feedback; the speed reference is $200rpm$, with fundamental frequency $f_e = 40/3Hz$. E_α , E_β , ω_e , θ_e (real value and estimated value), and all errors are shown in Fig. 3.3.

Though there are significant errors in $E_{\alpha_{est}}$, $E_{\beta_{est}}$, and $\omega_{e_{est}}$, $\theta_{e_{est}}$ matches with the real with

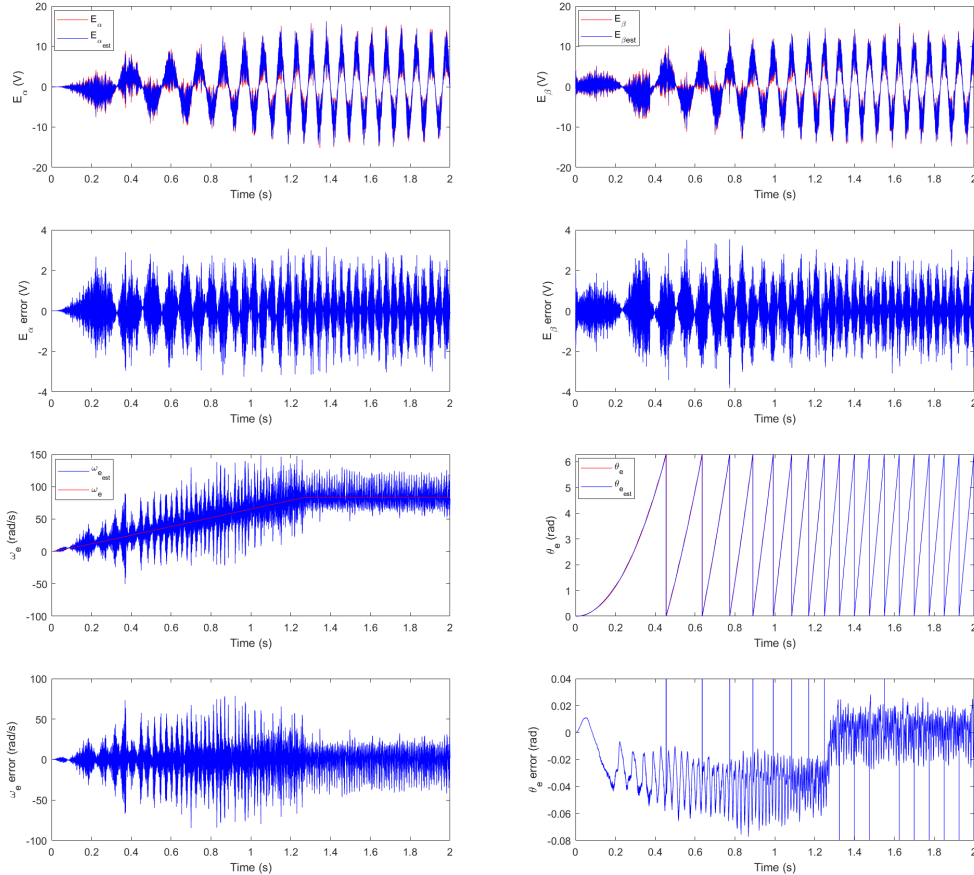


Figure 3.3: Real and estimated value of E_α , E_β , ω_e and θ_e

real value with $\tilde{\theta}_e$ constantly remains in the range of $[-0.06, 0.03]rad$, which proves that the

high-frequency noise in $\hat{E}_{\alpha\beta}$ leads to the error in estimated speed. Because of the inverter, high-frequency noise is injected into the observer, especially the back EMF, leading to a high-frequency noise in the estimated speed $\omega_{e_{est}}$. Though the three-level inverter and the filter mentioned in chapter 2 are designed to attenuate the harmonic generated by switching, the noise still leads to a significant error in the speed estimation. The FFT analysis of $E_{\alpha_{est}}$ is shown in Fig. 3.4. The THD of \hat{E}_{α} is 26.57%.

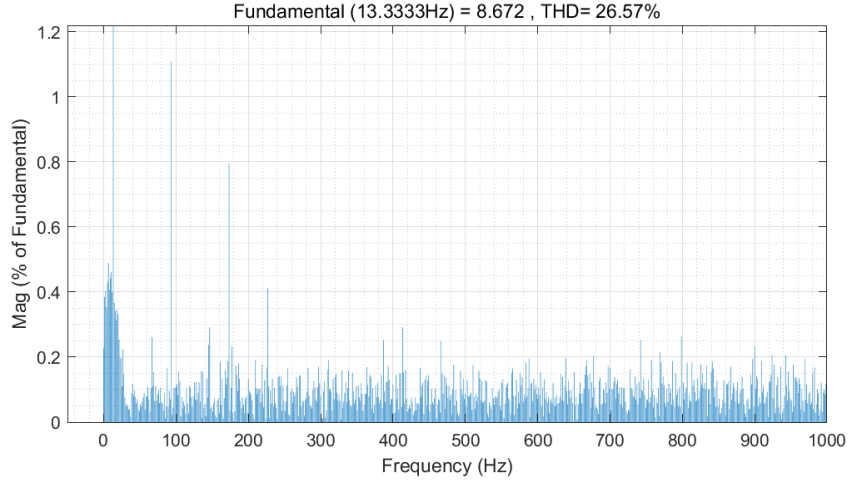
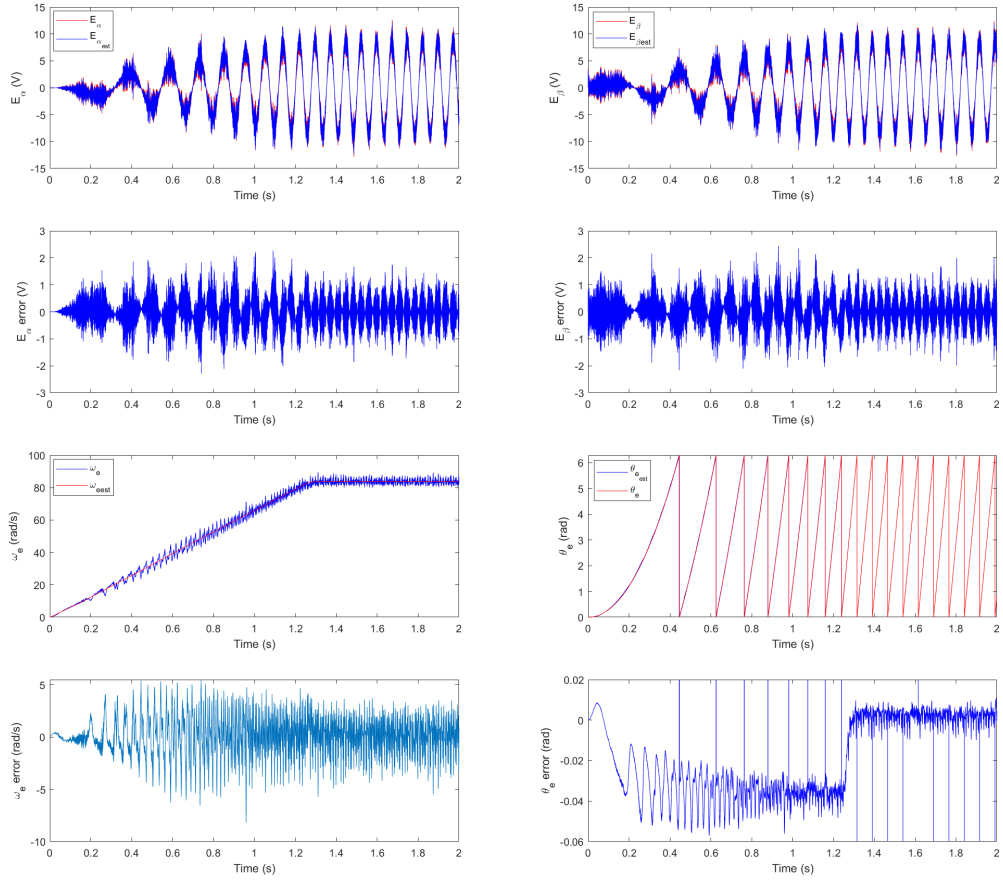


Figure 3.4: FFT analysis of $E_{\alpha_{est}}$

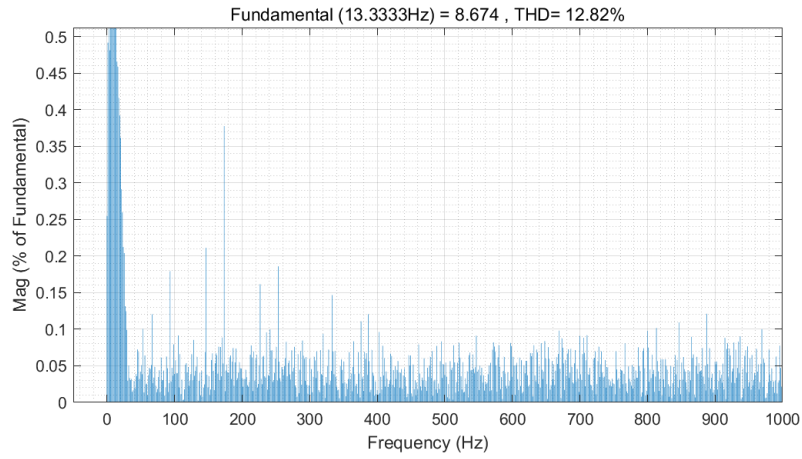
An adaptive low-pass filter is used in [20], [21] to attenuate the noise in back EMF estimation, which accepts the estimated fundamental frequency of IPMSM ω_e as the cut-off frequency.

$$\begin{cases} \hat{E}'_{\alpha} = LPF(\hat{E}_{\alpha}) = \frac{\hat{\omega}_e}{s + \hat{\omega}_e} \hat{E}_{\alpha} \\ \hat{E}'_{\beta} = LPF(\hat{E}_{\beta}) = \frac{\hat{\omega}_e}{s + \hat{\omega}_e} \hat{E}_{\beta} \end{cases} \quad (3.32)$$

The E_{α} , E_{β} , ω_e , and θ_e (real value and estimated value) of the filtered system are shown in Fig. 3.5(a). Compared with the unfiltered system, the error of $\hat{\omega}_e$ stays in the range of $[-5, 5]rad/s$ ($10rpm$) during the starting range, and drops to $[-2, 2]rad/s$ when speed reaches steady speed without an obvious phase delay. $\tilde{\theta}_e$ still remains in the range of $[-0.06, 0.03]rad$. The FFT of filtered \hat{E}_{α} is shown in Fig. 3.5(b), and the THD drops from 26.57% to 12.82%.



(a) Real and estimated value of E_{α} , E_{β} , ω_e and θ_e after adaptive low pass filter



(b) FFT analysis of $E_{\alpha_{est}}$ after adaptive low pass filter

Figure 3.5: Simulation result of a filtered SMO

After the test with real ω_e and θ_e feedback, the estimated $\hat{\omega}_e$ and $\hat{\theta}_e$ from SMO is used for IPMSM sensorless control. E_α , E_β , ω_e , θ_e (real value and estimated value), and all errors are shown in Fig. 3.6.

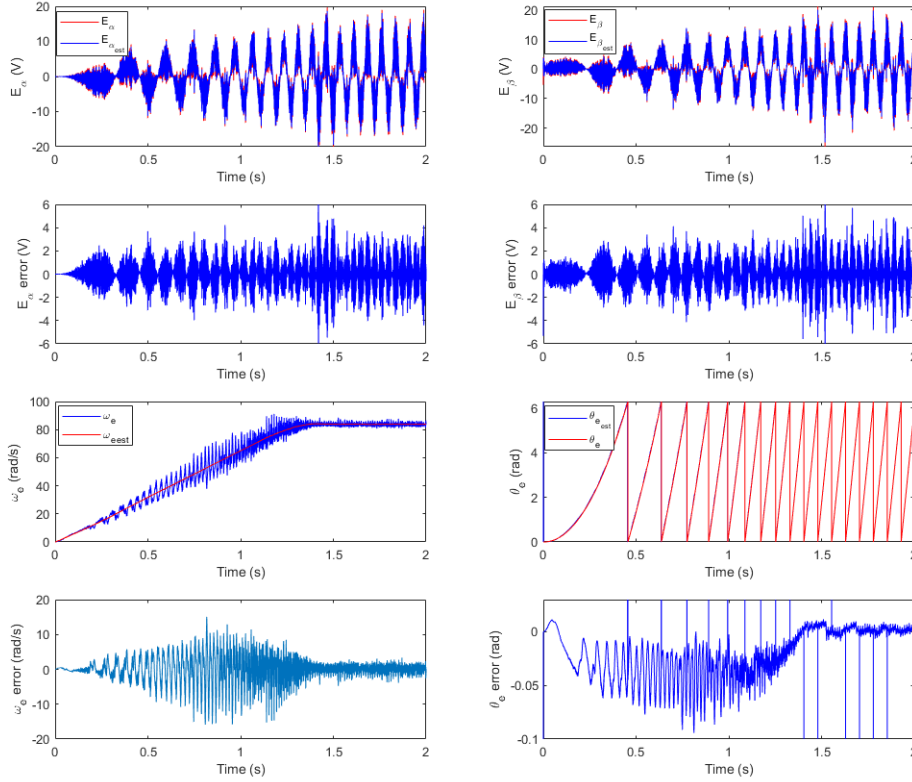


Figure 3.6: E_α , E_β , ω_e and θ_e with SMO sensorless control

Compared with actual speed and position feedback, the IPMSM can remain at a steady 200rpm speed with SMO-based sensorless control. The error of all estimated variables does not increase significantly, which proves that SMO sensorless control can be used on this IPMSM. Though there is still noise on the estimated speed, due to the speed and current controller, and the inertia of IPMSM, the noise does not reflect on the actual speed. Due to the phase delay generated by the low pass filter, there is some overshoot when speed reaches the reference speed, but the speed can return to the reference speed within 0.2s. However, the delay has a significant influence on the load test. When a $1N \cdot m$ load is applied after the IPMSM goes to the steady speed, the observer can not follow the speed, and the system lost stability.

3.4 IPMSM flux linkage nonlinear observer

At low and high speeds, the back EMF is not the same, leading to a prominent observer gain h to guarantee convergence. Nevertheless, a large observer gain introduces a lot of noise under low-speed conditions, which brings some adverse effects to the back EMF estimation, and further influences the speed estimation. The magnetic flux of the rotor is essentially similar, leading to a steady observer gain [4]. By observing the magnetic flux, the negative effects of low signal-to-noise ratio and nonlinear factors at low speeds can be avoided.

The $\alpha\beta$ IPMSM dynamic model is shown in Eq. 3.10, and we can rewrite this equation into:

$$\begin{bmatrix} u_\alpha \\ u_\beta \end{bmatrix} - R_s \begin{bmatrix} i_\alpha \\ i_\beta \end{bmatrix} = \begin{bmatrix} L_\alpha & L_{\alpha\beta} \\ L_{\alpha\beta} & L_\alpha \end{bmatrix} \frac{d}{dt} \begin{bmatrix} i_\alpha \\ i_\beta \end{bmatrix} + \begin{bmatrix} -\lambda_r \omega_e \sin(\theta_e) \\ \lambda_r \omega_e \cos(\theta_e) \end{bmatrix} \quad (3.33)$$

The left part of this equation is the back EMF, and the integration of the back EMF is the flux linkage. Therefore, we can define two state variables:

$$E = -R_s i_{\alpha\beta} + u_{\alpha\beta} \quad (3.34)$$

$$\frac{d\lambda}{dt} = L_s \frac{d}{dt} i_{\alpha\beta} - \omega_e \lambda_r \begin{bmatrix} \sin(\theta) \\ -\cos(\theta) \end{bmatrix} \quad (3.35)$$

where $E = \frac{d\lambda}{dt}$, and the flux linkage can be written into:

$$\lambda = L_s i_{\alpha\beta} + \lambda_r e^{j\theta_e} \quad (3.36)$$

where $\lambda = [\lambda_\alpha, \lambda_\beta]^T$. To construct a nonlinear observer, define a vector function $\varepsilon : \mathbb{R}^2 \rightarrow \mathbb{R}^2$

$$\varepsilon(\lambda) = \lambda - L_s i_{\alpha\beta} \quad (3.37)$$

and from Eq. 3.36 and Eq. 3.37, the Euclidean distance of the vector function is:

$$\| \varepsilon(\lambda) \|^2 = \lambda_r^2 \quad (3.38)$$

An error function of $\varepsilon(\hat{\lambda})$ can be written as $e(\hat{\lambda}) : \mathbb{R}^2 \rightarrow \mathbb{R}$

$$e(\hat{\lambda}) = (\| \varepsilon(\lambda) \|^2 - \| \varepsilon(\hat{\lambda}) \|^2)^2 = (\lambda_r^2 - \| \varepsilon(\hat{\lambda}) \|^2)^2 \quad (3.39)$$

Define the estimated rotor flux linkage as $\hat{\lambda}$, we can minimize the error $(\lambda_r^2 - \| \varepsilon(\hat{\lambda}) \|^2)$ by gradient descent method [22]:

$$\dot{\hat{\lambda}} = v_{\alpha\beta} - R_s i_{\alpha\beta} + \frac{\gamma}{4} \nabla_{\hat{\lambda}} \| \varepsilon(\hat{\lambda}) \|^2 e(\hat{\lambda}) \quad (3.40)$$

where γ is the gradient search factor and ∇ is the gradient operator. $\nabla_{\hat{\lambda}} = grad(\hat{\lambda}_\alpha, \hat{\lambda}_\beta) = [\partial/\partial\hat{\lambda}_\alpha, \partial/\partial\hat{\lambda}_\beta]^T$. Substituting Eq. 3.39 in to Eq. 3.40 yields:

$$\dot{\hat{\lambda}} = v_{\alpha\beta} - R_s i_{\alpha\beta} + \frac{\gamma}{4} \nabla_{\hat{\lambda}} \| \varepsilon(\hat{\lambda}) \|^2 [\lambda_r^2 - \| \varepsilon(\hat{\lambda}) \|^2] \quad (3.41)$$

The observer in Eq. 3.41 can be simplified into:

$$\dot{\hat{\lambda}} = v_{\alpha\beta} - R_s i_{\alpha\beta} + \frac{\gamma}{2} \varepsilon(\hat{\lambda}) [\lambda_r^2 - \| \varepsilon(\hat{\lambda}) \|^2] \quad (3.42)$$

Rewrite Eq. 3.36 into:

$$\frac{1}{\lambda_r} (\lambda - L_s i_{\alpha\beta}) = e^{j\theta} = \begin{bmatrix} \cos(\theta_e) \\ \sin(\theta_e) \end{bmatrix} \quad (3.43)$$

Replace θ_e with $\hat{\theta}_e$, and we can have the estimated angle from the observer by:

$$\begin{bmatrix} \cos(\hat{\theta}_e) \\ \sin(\hat{\theta}_e) \end{bmatrix} = \frac{1}{\lambda_r}(\hat{\lambda} - L_s i_{\alpha\beta}) \quad (3.44)$$

Define the observation error as $\tilde{\lambda} = \hat{\lambda} - \lambda$, the error can be expressed into :

$$\dot{\tilde{\lambda}} = -\gamma \left[\frac{1}{2} \|\tilde{\lambda}\|^2 + \lambda_r [\tilde{\lambda}_\alpha \cos(\theta) + \tilde{\lambda}_\beta \sin(\theta)] \right] \left\{ \tilde{\lambda} + \lambda_r \begin{bmatrix} \cos(\theta) \\ \sin(\theta) \end{bmatrix} \right\} \quad (3.45)$$

and this error is shown in [17] satisfying global stability propriety: for $\hat{\lambda} \in \mathbb{R}^2$, we have $\|\hat{\lambda}\| / \leq 2\lambda_r$. Therefore, all trajectories of the error in Eq. 3.45 will always be attracted to the dist.

Similarly, a phase lock loop will help with the angle and speed extraction, which can be expressed into:

$$\hat{\theta}_e = \tan^{-1} \left(\frac{\hat{\lambda}_\beta - L_s i_\beta}{\hat{\lambda}_\alpha - L_s i_\alpha} \right) \quad (3.46)$$

3.5 Flux observer sensorless control simulation & Comparison between flux observer and SMO

The same simulation shown in Fig. 3.2 is used in the flux observer test, also with a 200rpm reference mechanical speed. λ_α , λ_β , ω_e , θ_e (real value and estimated value), and all errors are shown in Fig. 3.7.

The error of $\hat{\lambda}_{\alpha\beta}$ remains at $6e-5Wb$, and the error of ω_e remains in the range of $[-1, 1]rad/s$, while the error of θ_e is $0.2rad$ in the starting stage and drops to $0.005rad$ when the IPMSM stops accelerating and reaches reference speed.

Compared with the back EMF, $\lambda_{\alpha\beta}$ has almost no high-frequency noise. The FFT of λ_α is

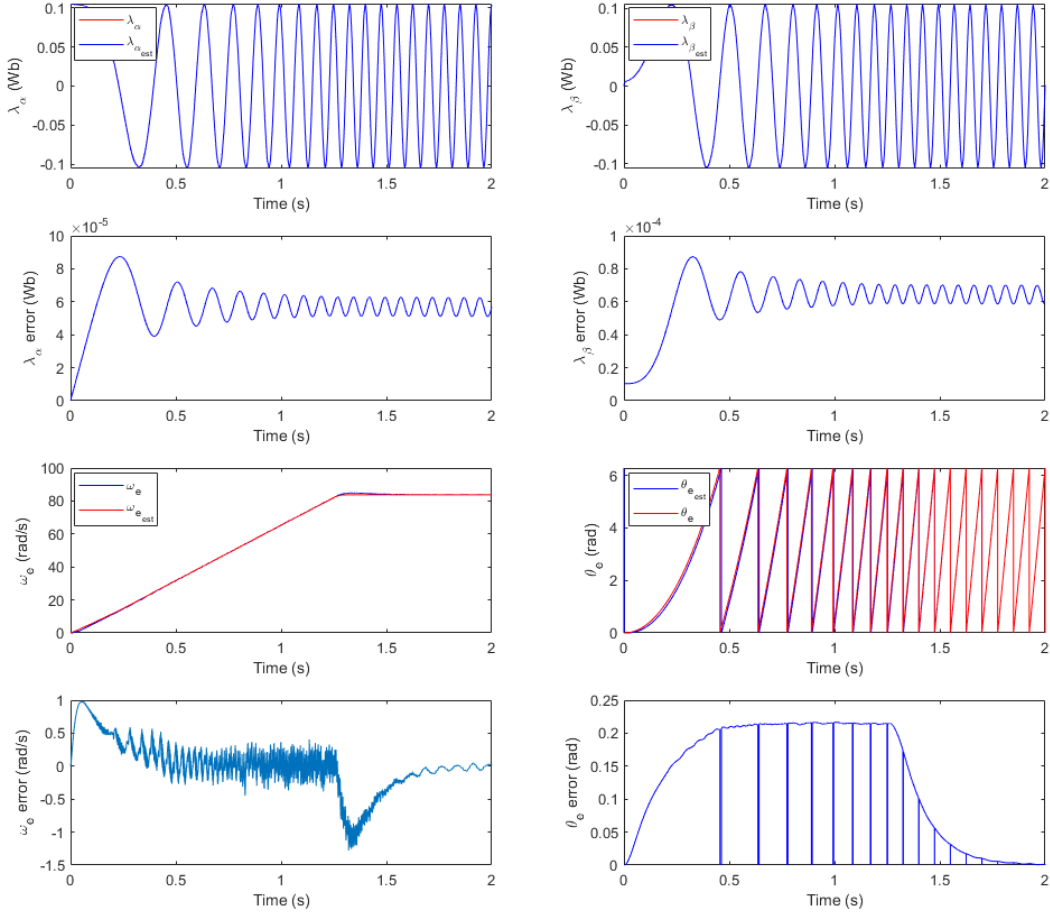


Figure 3.7: Real and estimated value of λ_α , λ_β , ω_e and θ_e

shown in Fig. 3.8. THD is only 0.9%, while the magnitude of the fundamental frequency component is $0.1034Wb$, which matches with the flux linkage λ_r . Furthermore, the flux linkage observer only accepts $\hat{\theta}_e$ as the input to compute the inductance matrix L_s , and $\hat{\omega}_e$ is extracted by phase lock loop; while SMO needs $\hat{\omega}_e$ to estimate the back EMF. In the phase lock loop, the angle is computed by integrating the speed, which filters obvious noise on the estimated speed $\hat{\omega}_e$. Therefore, $\hat{\theta}_e$ always tends to have less noise than $\hat{\omega}_e$. These properties give the flux observer better robustness, dynamics, and noise-against capability.

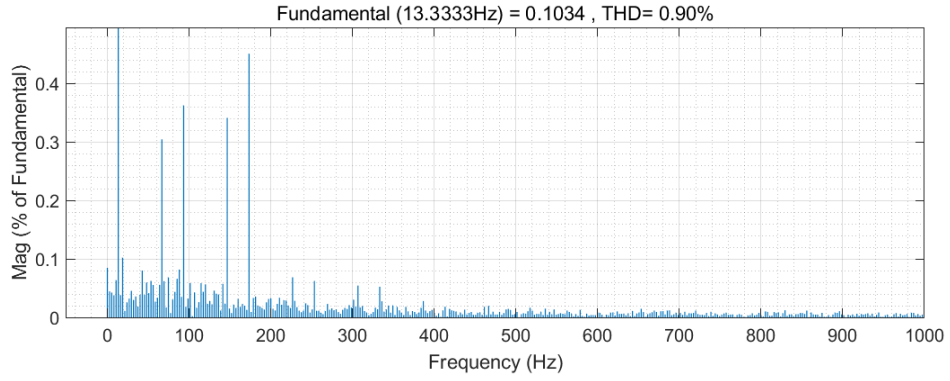


Figure 3.8: FFT analysis of $\lambda_{alpha_{est}}$

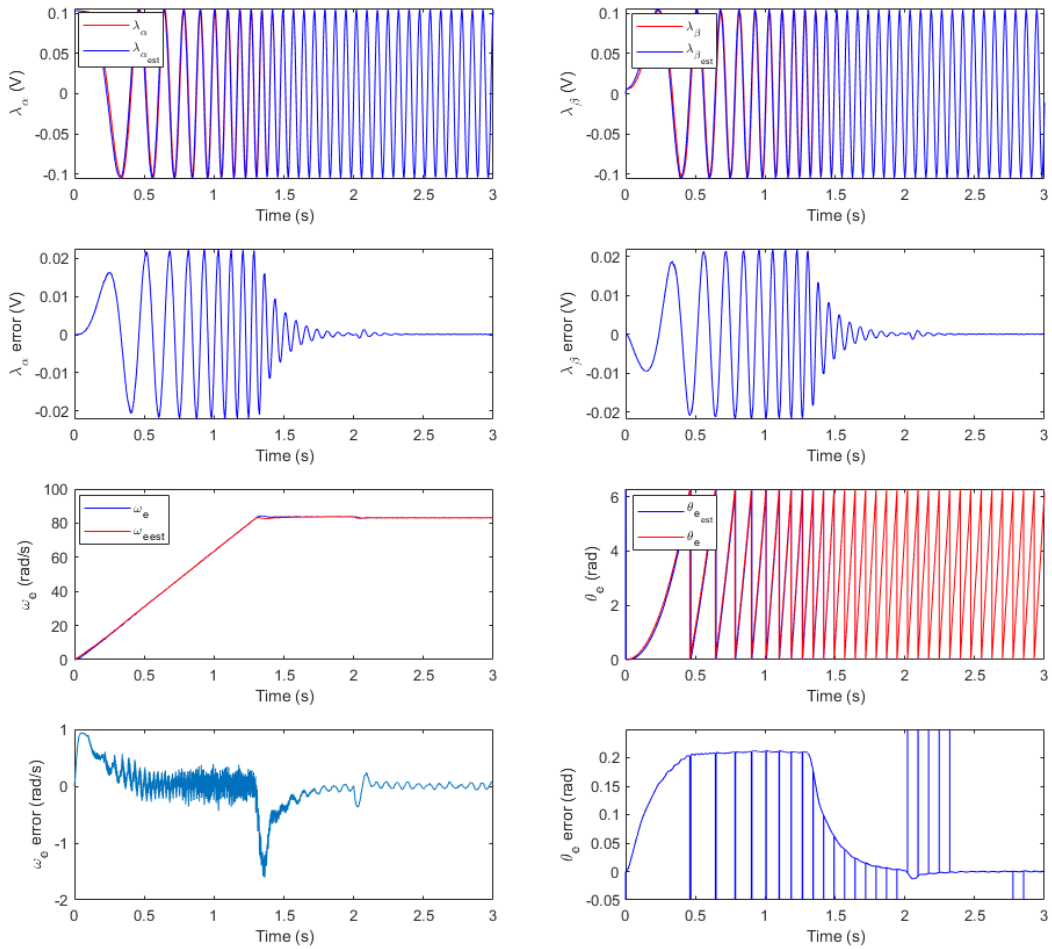


Figure 3.9: E_{α} , E_{β} , ω_e and θ_e with flux observer sensorless control

The sensorless control is simulated for the flux observer. $\lambda_\alpha, \lambda_\beta, \omega_e, \theta_e$ (real value and estimated value), and all errors are shown in Fig. 3.9.

Compared with real position and speed feedback, estimated flux linkage $\hat{\lambda}_{\alpha\beta}$ shows a $0.02Wb$ error. However, the error of estimated speed and angle does not change. Furthermore, because of the lack of a low-pass filter, the speed response of flux-based sensorless control performs better. The real speed of IPMSM can go to reference speed without an obvious overshoot and the error of estimated θ_e can drop to almost 0 at steady state.

A load test is also simulated. A $1N \cdot m$ load torque is applied at $2s$ after the IPMSM settles to reference speed. Due to the working essence of an IPMSM, the flux linkage does not change significantly with the torque. Therefore, the error of $\hat{\lambda}_{\alpha\beta}$ after load torque is around $0.0001Wb$, which can nearly be neglected, leading to excellent response and robustness on speed estimation. From the simulation, the flux-based sensorless control strategy has good low-speed accuracy and load capability.

3.6 Comparison between SMO and flux-based sensorless control strategy

In conclusion, a back EMF-based sliding mode observer is a type of nonlinear observer that uses a sliding mode control approach to estimate the back EMF of an IPMSM. While sliding mode observers have some advantages over other observers, such as robustness and accuracy, they also have disadvantages. Here are some specific weaknesses of a sliding mode observer sensorless control:

- Chattering: One of the main drawbacks of sliding mode observers is that they can exhibit chattering behavior, which is a high-frequency oscillation in the estimated position and speed of the motor. This can result in increased noise and vibration, and lead to excessive control efforts in the system. Furthermore, back EMF is also a high-frequency signal, which aggravates this drawback.

- Weak noise-against capability: SMO can be sensitive to measurement noise and disturbances, leading to errors in the estimated position and speed of the motor. This can affect the overall performance of the control system and may require additional filtering or signal processing.
- Weak load capability: The SMO-based sensorless control system is fragile, especially at low-speed condition. A sudden load will likely introduce too much noise and lead to system instability.
- Tuning difficulties: Tuning a sliding mode observer can be difficult, especially if the system dynamics are complex. The observer gain parameters must be carefully tuned to achieve the desired performance, which can be time-consuming and iterative. And back EMF is almost linear to the speed, leading to a contradictory tradeoff between low-speed inaccuracy and high-speed saturation.
- High sensitivity to modeling errors: Sliding mode observers are highly sensitive to modeling errors, especially if the system dynamics are highly nonlinear. This can lead to inaccurate state estimates and poor system performance.

There are some specific advantages of flux linkage observer over back EMF sliding mode observer:

- Improved low-speed performance: Flux linkage observers are generally more effective at low speeds, where the back EMF is weak and can be challenging to measure accurately. In contrast, back EMF sliding mode observers may have difficulty accurately estimating the rotor position and speed at low speeds. Furthermore, the magnitude of flux linkage is almost constant in all speed ranges, and we can easily find an appropriate gain for the flux observer which can consider both low-speed accuracy and high-speed saturation.
- Improved load performance: Flux linkage observers are generally more effective when a sudden load is applied because the flux linkage does not change significantly in an

IPMSM when torque changes. Furthermore, flux observer control is less sensitive to variations in motor parameters such as resistance and inductance, which can vary with load conditions. This allows for better performance and stability under varying load conditions.

- More accurate estimation: Flux linkage observers can provide more accurate estimates of the rotor position and speed than back EMF sliding mode observers, especially in applications where the motor parameters are unknown or change over time. This is because flux linkage observers use a more direct measurement of the rotor position and speed, whereas back EMF sliding mode observers rely on indirect measures.
- Reduced complexity: Flux linkage observers are often simpler to implement than back EMF sliding mode observers, since they require fewer measurements and fewer control parameters. This can make them more practical for some applications, especially those with limited computational resources or real-time constraints.

Overall, flux linkage observers have several advantages over back EMF sliding mode observers for estimating the rotor position and speed of a PMSM, including improved low-speed performance, more accurate estimation, greater robustness, and reduced complexity.

Chapter 4

A starting strategy for sensorless IPMSM

The above chapters demonstrated the T-type inverter and flux linkage observer. However, the flux linkage observer is unstable at starting stage. Therefore this chapter will discuss how to start the motor from open-loop control.

4.1 Transition between open and closed-loop control

To start an IPMSM, a current with gradually increasing frequency is applied to the stator winding to create a rotating magnetic field with a closed current loop, which causes the rotor to start rotating. The frequency should be determined by the speed of the motor, which the flux linkage observer estimates. However, at starting stage, the observer can not accurately estimate ω_e and the rotor position θ_e . Therefore, an open loop I-f starting strategy is usually applied for motor starting [23].

The advantage of this method is that it is simple and does not require any feedback control. However, the motor performance and the load on the motor may change during the starting process, which may affect the accuracy of the speed control. Therefore, this method is typically used for applications where the load on the motor is constant and the

speed control requirements are not stringent.

In open loop I-f starting, the current is applied to the stator winding with a current regulator, and the frequency of the current is increased gradually until the desired speed is reached. The frequency is raised at a linear speed, while the voltage is kept constant until the frequency reaches a particular value. This process is repeated until the motor reaches the desired speed. When the speed is high enough to support the flux linkage observer to generate a valid estimation, a smooth transition is necessary to assist the speed controller to join the control, and after the transition, the IPMSM will be driven in a completely closed loop.

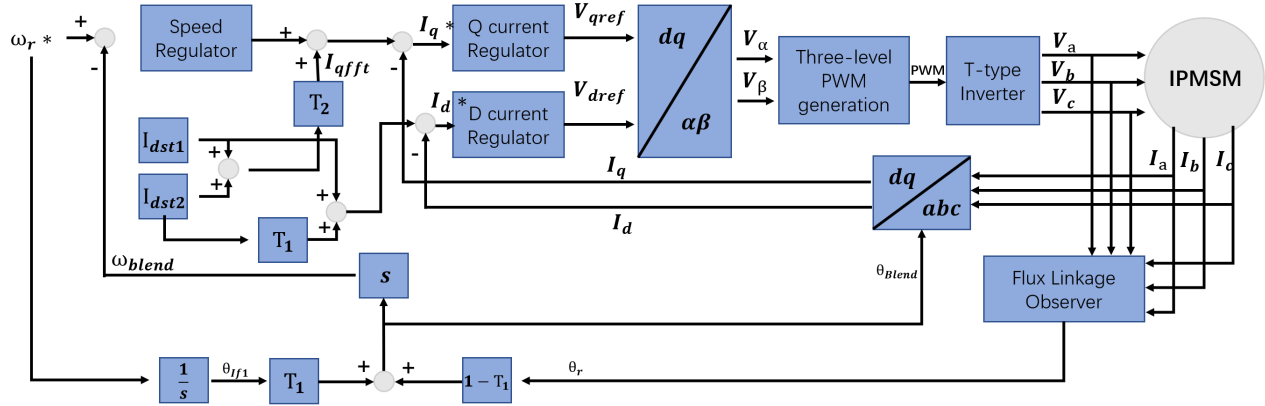


Figure 4.1: Block diagram of the proposed blending transition strategy

During the I-f start-up stage, the reference speed ω_r is generated by using a linear signal generator, while a current is added on the d-axis of $I-f$ coordinate with magnitude $I_{dif} = I_{dst1} + I_{dst2}$. With the rotation of this current, a projection of I_{dif} on the real q-axis will drive the rotor to rotate. Therefore, we can have two d-q axis, namely dq_{IPM} and dq_{If} . When the speed of IPMSM (reference speed ω_r) reaches enough speed for the observer, a blending strategy will transfer from I-f control to speed regulator control. The diagram is shown in Fig. 4.1.

Before the transition starts, the speed feedback is directly speed reference ω_r^* , which aims to avoid error accumulation in the speed controller, while theta θ_{If1} is computed by integration of speed reference. Hence, we can have an I-f reference dq_{If1} . The current reference I_{dIf1} is a given fixed number $I_{dst1} + I_{dst2}$. and the projection of I_{dIf1} on q_{IPM} will generate a torque to drive the IPMSM.

When the transition happens, two transition coefficients T_1 and T_2 will blend the theta from the integration theta θ_{If1} and the observer estimated theta $\hat{\theta}_r$. T_1 will gradually decrease from 1 to 0, which tunes the weight of two thetas in the feedback. At the same time, T_2 will increase from 0, leading to a I_{qst} on dq_{If1} to maintain the torque. When T_1 drops to 0, we can have a new reference dq_{If2} , with $I_{dIf2} = I_{dst1}$ and $I_{qIf2} = T_2 I_{qst}$. I_{qIf2} will provide most of the torque, while I_{dIf2} will maintain the magnetic field to stabilize the transition and avoid the nonalignment. The phasor diagram is shown in Fig. 4.2.

The feedback theta $\theta_{blend} = T_1 \theta_{If1} + (1 - T_1) \theta_r$, as well the speed $\omega_{blend} = T_1 \omega_{If1} + (1 - T_1) \omega_r$.

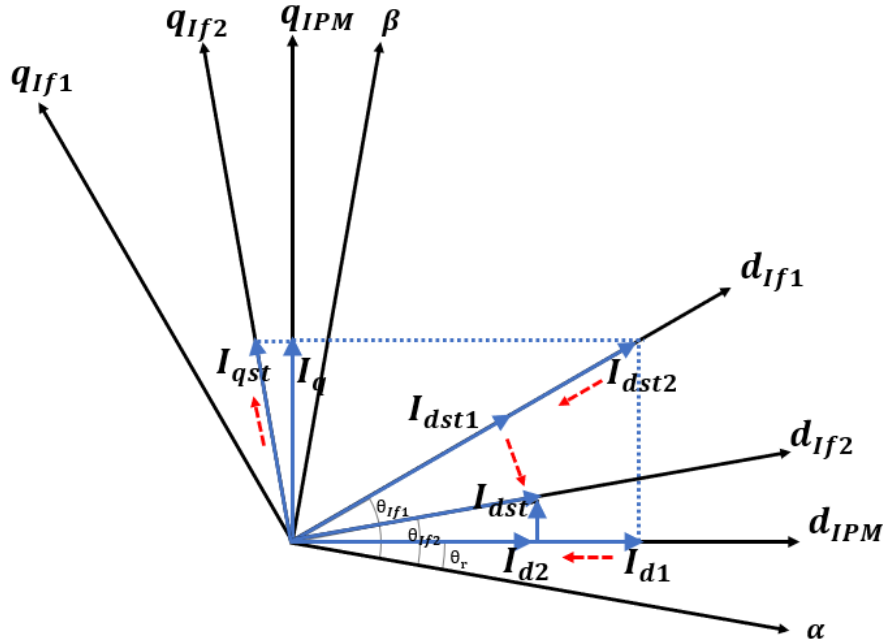


Figure 4.2: Phasor diagram of the transition process from I-f to closed loop

The theta difference between dq_{If} and dq_{IPM} is expressed into $\theta_T = \theta_{If1} - \theta_{IPM}$. The blending current are $I_{dIf} = I_{dst1} + T_1 I_{dst2}$ and $I_{qIf} = T_2 (I_{dst1} + I_{dst2})$. Therefore, we can have the torque

expressed into:

$$T_e = \frac{3}{2}p\lambda_r[(I_{dst1} + T_1 \cdot I_{dst2})\sin(T_1\theta_T) + T_2(I_{dst1} + I_{dst2})\cos(T_1\theta_T)] \quad (4.1)$$

To maintain the torque during the process, we should have $T_e = T_e(0)$, where $T_1 = 1$, $T_2 = 0$:

$$T_e(0) = \frac{3}{2}p\lambda_r(I_{dst1} + I_{dst2})\sin(\theta_T(0)) \quad (4.2)$$

Thus, we can compute T_2 by:

$$T_2 = \frac{(I_{dst1} + I_{dst2})\sin(\theta_T(0)) - (I_{dst1} + T_1 \cdot I_{dst2})\sin(T_1\theta_T(t))}{(I_{dst1} + I_{dst2})\cos(T_1\theta_T(t))} \quad (4.3)$$

Where $\theta_T(0)$ is the angle difference between dq_{IPM} and dq_{IF} when the transition starts and does not change during the transition. When T_1 drops to 0, the dq_{IF} will overlap with the real dq axis, where $I_{dref} = I_{dst1}$ and $I_q = (I_{dst1} + I_{dst2})\sin(\theta_T(0))$.

With the smooth transition strategy, we can avoid the torque ripple generated by a sudden change in the rotor position feedback. Furthermore, a d - axis current is maintained to stabilize the alignment.

4.2 Simulation of the transition strategy

The transition strategy is simulated in Simulink. A linear increasing speed reference is given at the starting stage. A transition command is given when the IPMSM speed reaches the expected speed reference. and in the simulation, we choose 200rpm as the transition speed to guarantee that the flux linkage observer can give a valid speed and rotor position estimation. Then the transition coefficient T_1 and T_2 will blend the open-loop and estimated position θ_e , mechanical speed ω_m , and electrical speed ω_e .

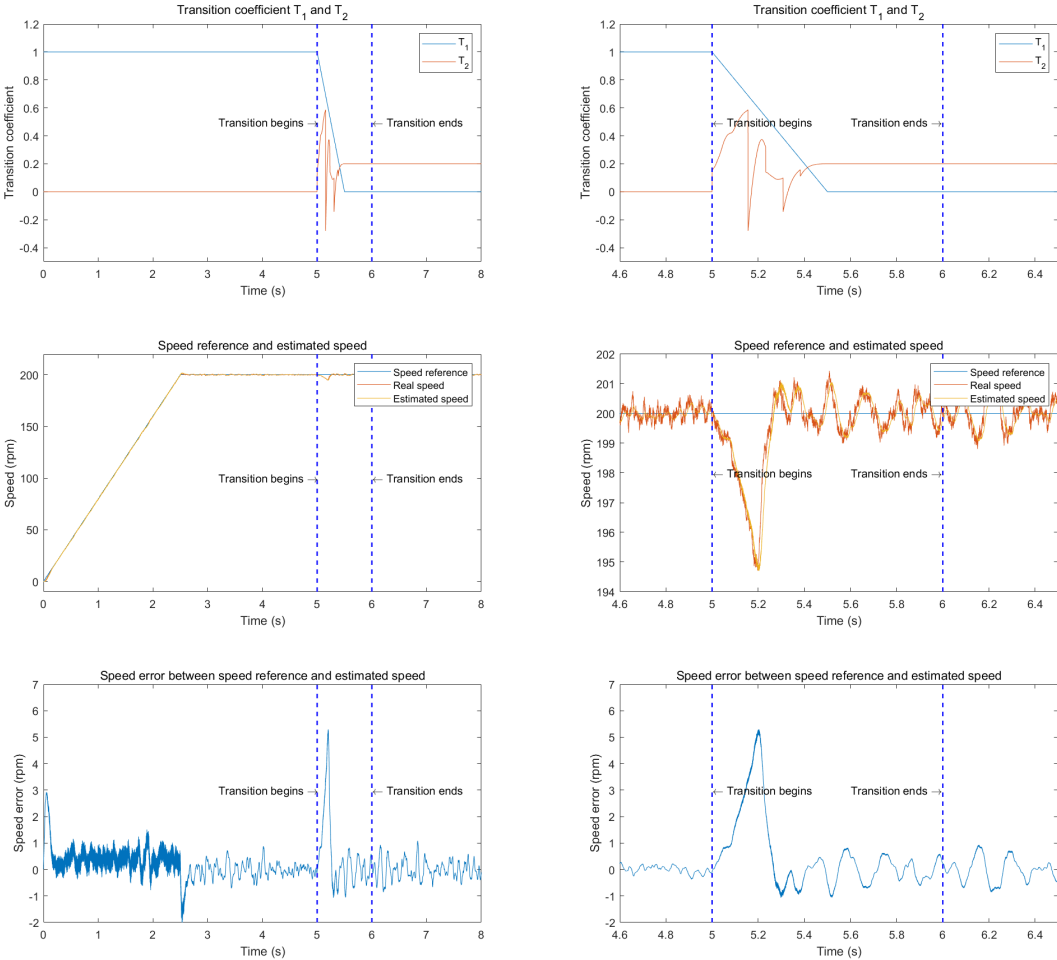


Figure 4.3: Transition coefficient, motor speed, and speed error during transition

During the process, T_1 will decrease to 0 from 1, while the d-axis current reference will decrease from $I_{dst1} + I_{dst2}$ to I_{dst1} . Meanwhile, the q-axis current will increase from 0 to $T_2(I_{dst1} + I_{dst2})$. The simulated transition T_1 , T_2 , and IPMSM speed are shown in Fig. 4.3. The duration of the transition process is from 5s to 6s. During the transition, the maximum speed error is $5rpm$, and the average speed error is $1rpm$.

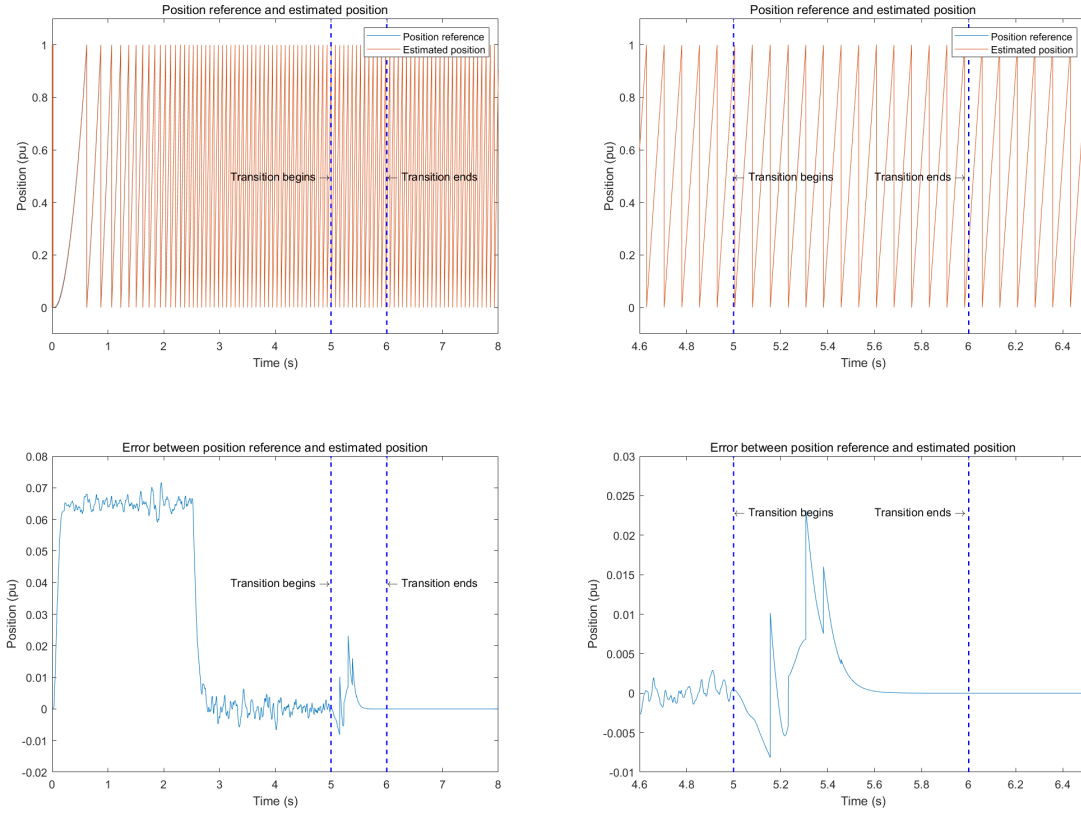


Figure 4.4: Rotor position, estimated rotor position and position error during transition

An intuitional assumption is the blending rotor position θ_e leads to vibration during the transition. However, because of the d-axis current, we can still maintain the alignment, and after the estimated position decouples with the real position, the error is eliminated. This assumption can be proved by the transition coefficient T_2 . The maximum speed error happens at 5.2s, and T_2 changes to a negative value, which means a negative q-axis current. Based on the strategy, T_2 should always keep positive to maintain the torque. The sudden drop in T_2 leads to a negative torque, and the motor decelerates at that moment. However, the

open-loop control still wants to keep the current frequency at $13.3Hz$, which is corresponding to $200rpm$. After the estimated d-q reference coincides with the real reference, the q-axis current goes back to normal value, and the motor can work with the feedback from the observer. The figure of estimated position and position error is shown in Fig. 4.4.

After the simulation of the transition strategy, the experimental validation of the entire system will be demonstrated in the next chapter.

Chapter 5

Experiment

This chapter discusses the design and testing of the hardware prototype of the three-level T-type inverter and sensorless control algorithm of an IPMSM. The experiment setup is shown in Fig. 5.1.

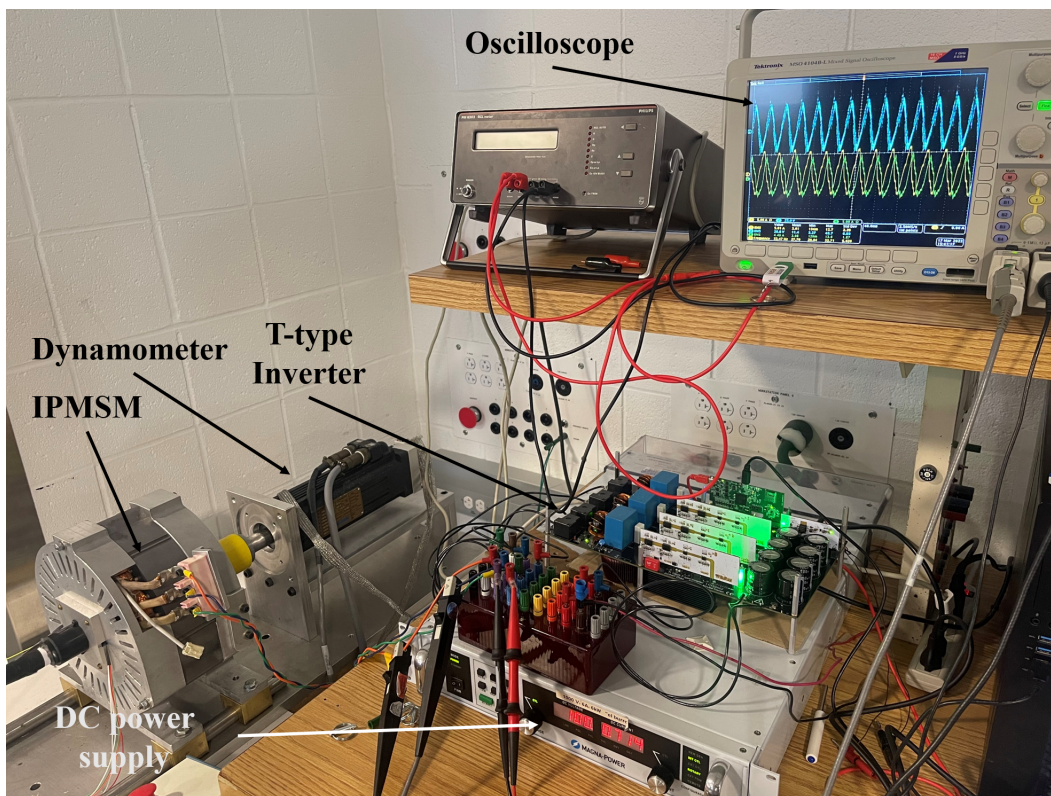


Figure 5.1: Experiment setup for IPMSM sensorless control

The communication between the inverter and computer is through a *TI28379D* control card, and the IPMSM parameter is shown in Table. 5.1.

Table 5.1: Experiment IPMSM parameters

Parameter	Value	Parameter	Value
λ_r	0.1034wb	R_s	0.0592 Ω
p	4	J	0.08kgm ²
L_d	0.845mH	L_q	2.217mH
B	0.16Ns/m		

5.1 Inverter DC test

This section will present the DC test with an open circuit and an LR load. The open circuit is done with a variable V_d command and $\theta_e = 0$, which is equivalent to connecting phase A to DC+, and connecting phase B and C to DC-. When $V_{dc} = 100V$, $\theta_e = 0$, the phase AB line-line unfiltered voltage is shown in Fig. 5.2.

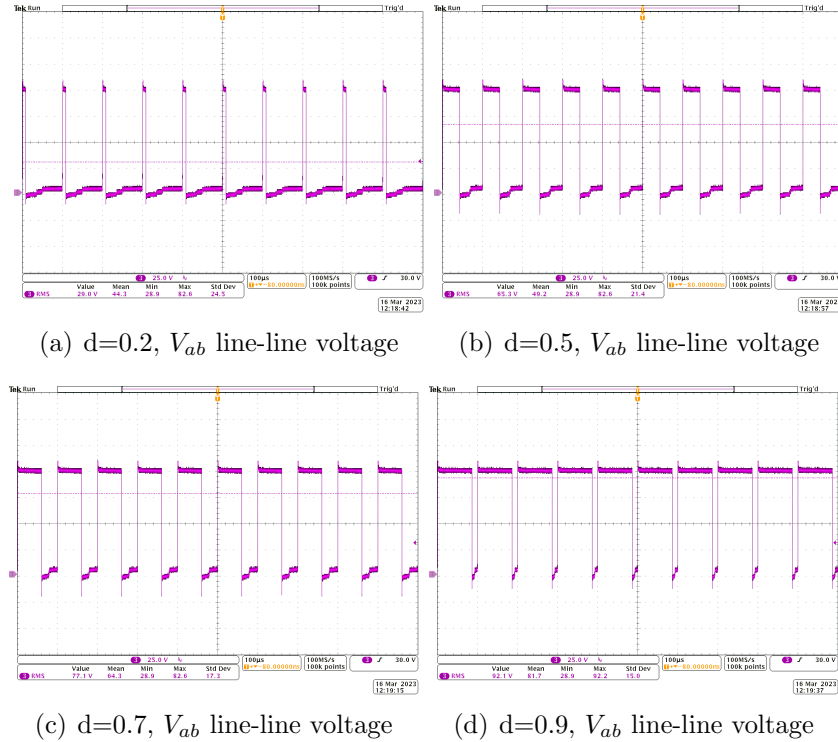


Figure 5.2: DC open circuit test without LCL filter (All curves are V_{ab})

With the increase of V_d , an increase in duty ratio is shown in the unfiltered PWM voltage, and the RMS value of the PWM voltage is equal to $V_d \times V_{dc}$.

Then with the same circuit, a filtered voltage after the LCL filter is shown in Fig. 5.3. Due to the lack of load, and the filter is not designed to filter a square to a DC output, the filtered voltage is not a perfect DC voltage, but we can still see a relatively DC output voltage.

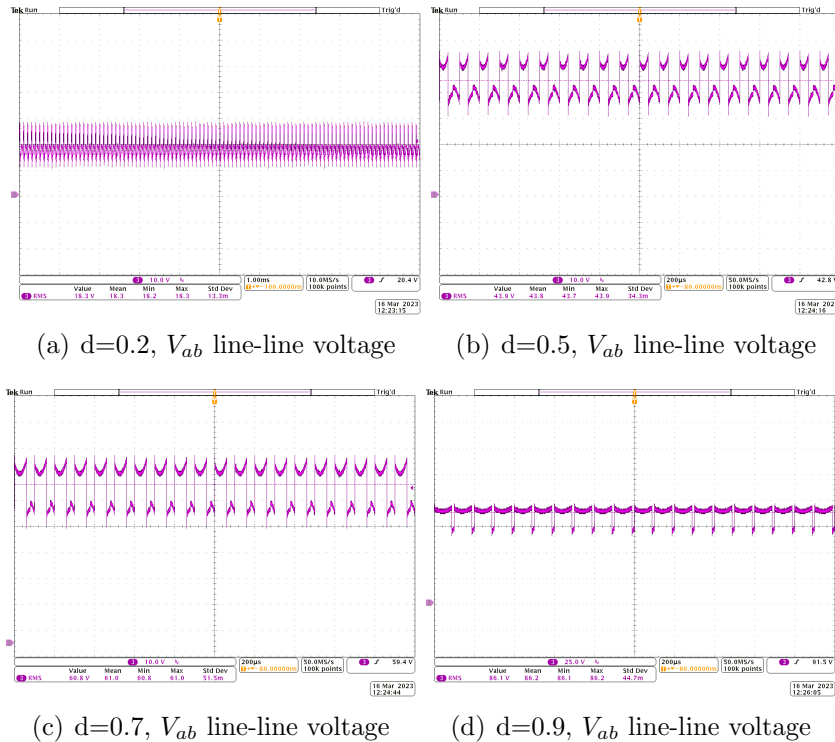


Figure 5.3: DC open circuit test with LCL filter (All curves are V_{ab})

The following is a dc test with LR load. The LR load is a 10Ω resistor and a $35mH$ inductor. The LR load test equivalent circuit is shown in Fig. 5.4. The load test still uses $V_{dc} = 100V$.

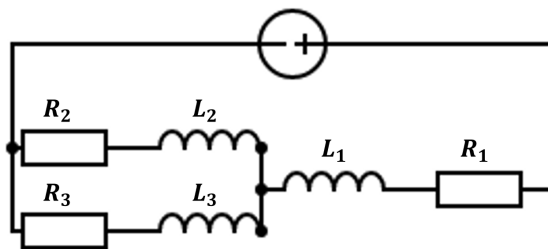


Figure 5.4: DC LR load test equivalent

The phase AB line-line voltage, phase A, B current is shown in Fig. 5.5. The purple curve is AB line-line voltage, the blue curve is phase A current, and the green curve is phase B current. When $V_d = 0.5$, the filtered $V_{ab} = 38.6V$. $I_a = \frac{V_{ab}}{R_{abc}} = \frac{38.6V}{15\Omega} = 2.57A$, and $I_b = -\frac{I_a}{2} = -1.28A$, which match with the RMS value from the oscilloscope.

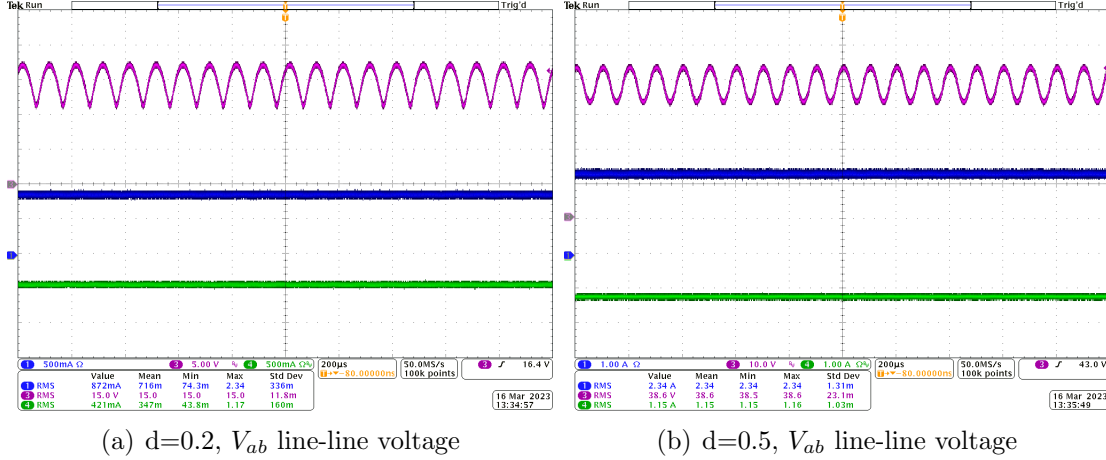


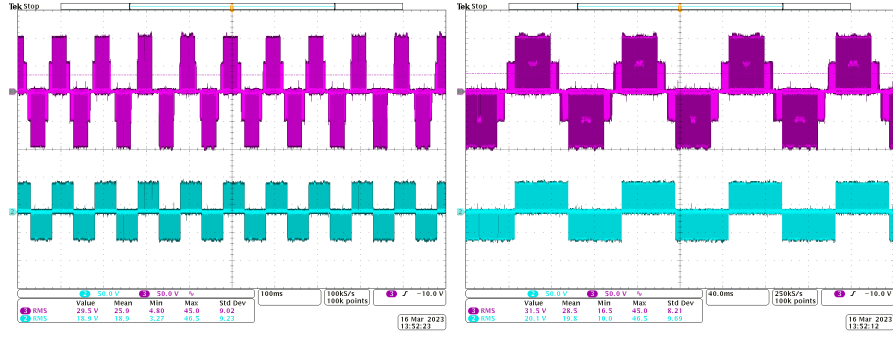
Figure 5.5: DC LR load test with LCL filter (Purple curves are V_{ab} , blue curves are I_a , green curves are I_b)

5.2 Inverter AC test

The phase A voltage V_a and line-line voltage V_{ab} of an open circuit AC test without an LCL filter are shown in Fig. 5.6. The DC link voltage $V_{DC} = 100V$, V_d varies from 0.2 to 0.9. The electrical angle θ_e is generated by integrating a fixed frequency $f_e = 10Hz$.

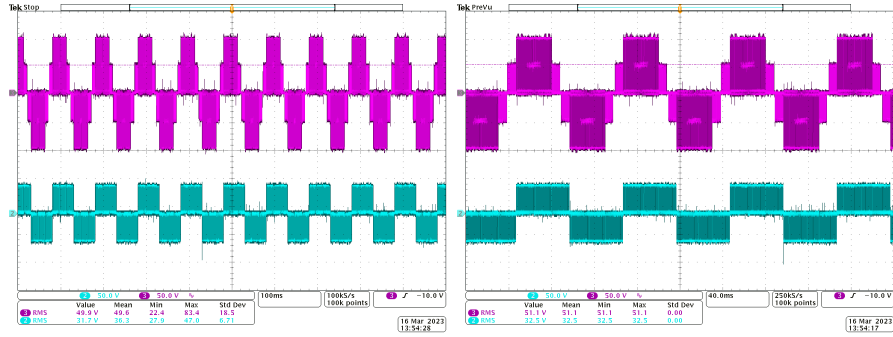
With different V_d , the phase voltage V_a always shows three levels with $DC+$, $DC-$, and 0, which leads to a five-level output line-line voltage, and the voltage waveform matches with the simulation shown in Fig. 2.11.

The filtered line-line voltage and phase voltage are shown in Fig. 5.7. The line-line voltage is a sinusoidal voltage with $10Hz$, and the magnitude changes with the V_d . Additionally, in Fig. 5.7(e), the phase voltage is similar to a third harmonic injection, which proves the successful deployment of SVPWM.



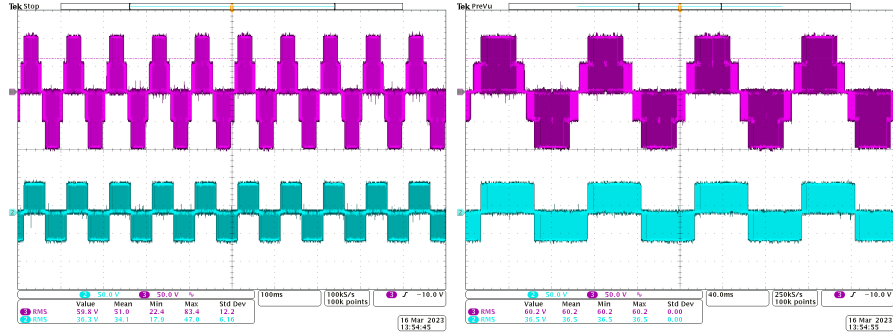
(a) $d=0.2$, V_{ab} line-line voltage

(b) $d=0.2$, V_{ab} line-line voltage



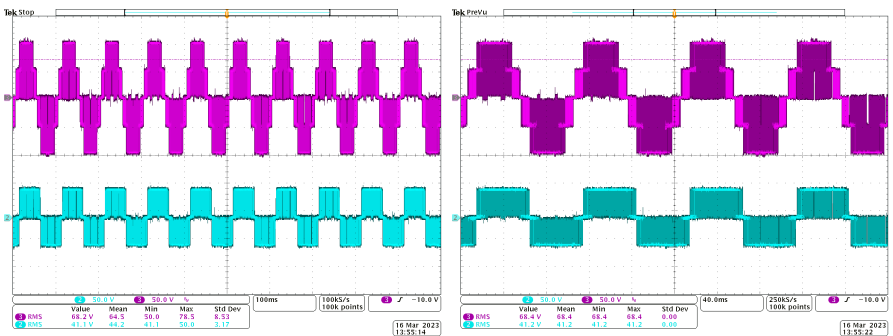
(c) $d=0.5$, V_{ab} line-line voltage

(d) $d=0.5$, V_{ab} line-line voltage



(e) $d=0.7$, V_{ab} line-line voltage

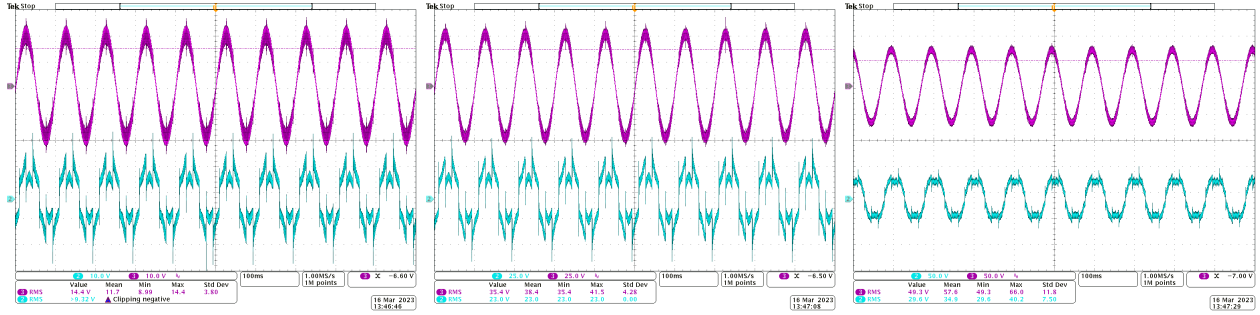
(f) $d=0.7$, V_{ab} line-line voltage



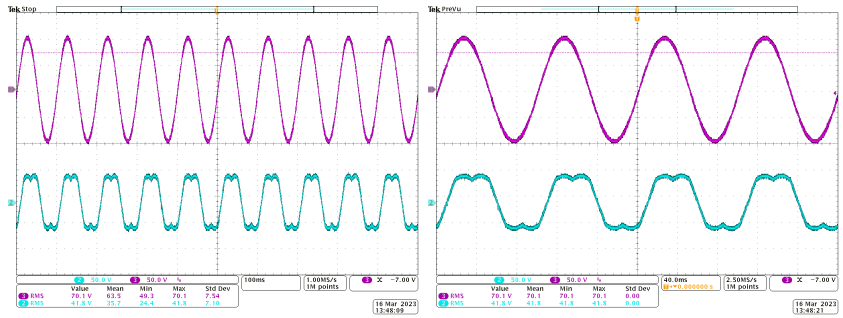
(g) $d=0.9$, V_{ab} line-line voltage

(h) $d=0.9$, V_{ab} line-line voltage

Figure 5.6: AC open circuit test without LCL filter (Purple curves are V_{ab} , blue curves are V_a)



(a) $d=0.2$, V_{ab} line-line voltage (b) $d=0.5$, V_{ab} line-line voltage (c) $d=0.7$, V_{ab} line-line voltage



(d) $d=0.9$, V_{ab} line-line voltage (e) $d=0.9$, V_{ab} line-line voltage

Figure 5.7: AC open circuit test with LCL filter (Purple curves are V_{ab} , blue curves are V_a)

The RL load AC test circuit is the same to the DC test circuit shown in Fig. 5.4. The line-line voltage and phase current of the AC LR load test when $V_d = 0.2$ is shown in Fig. 5.8.

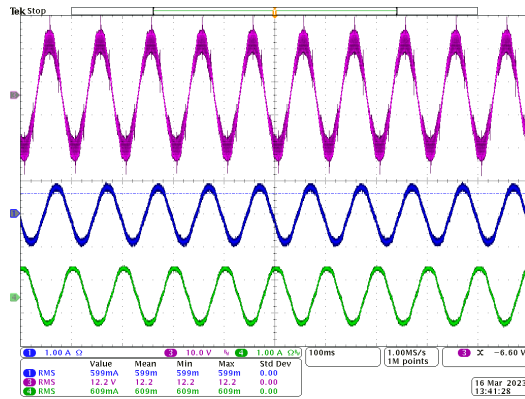


Figure 5.8: AC LR load test with LCL filter when $d=0.2$ (Purple curve is V_{ab} , blue curve is I_a , green curve is I_b)

5.3 Flux linkage observer test

The I-f open loop starting is utilized to test the flux linkage observer’s performance. This section will present two different operations with a step speed command and a linear increasing speed command. The line-line voltage V_{ab} , phase current I_a , estimated flux linkage $\lambda_{\alpha\beta}$, estimated speed ω_m and estimated rotor position θ_e are used to justify the transition.

Step speed reference

A step speed command is given to the I-f open loop signal generator, and the IPMSM will be dragged to rotate. The speed reference increases from 0 to 250 rpm and then decreases to 100 rpm. The phase AB line-line voltage and phase A current are shown in Fig. 5.9.

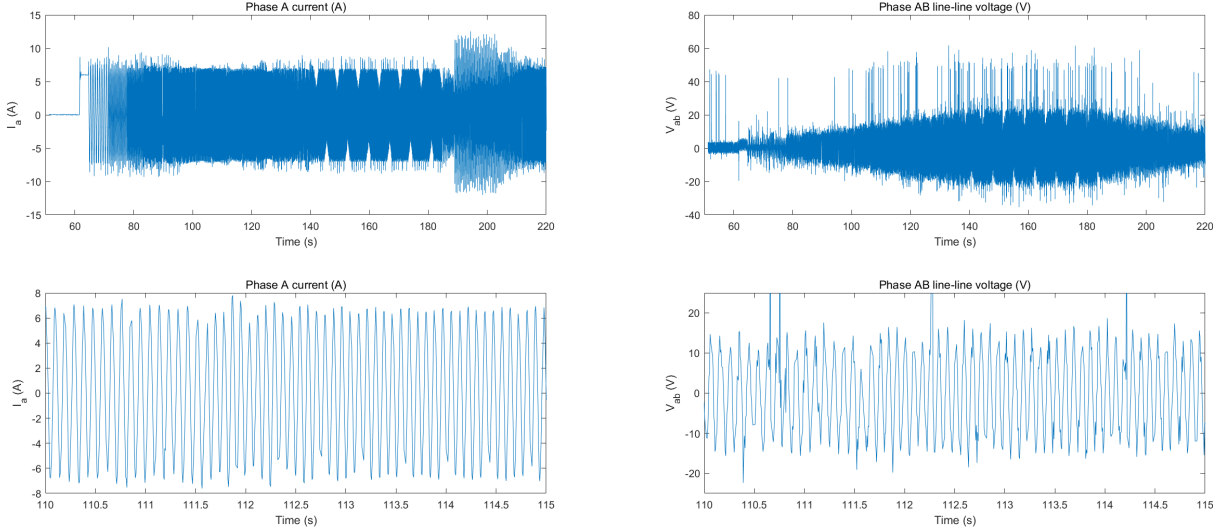


Figure 5.9: Phase current and line-line voltage during step I-f starting stage

The magnitude of phase voltage increases with the increase of speed, while the magnitude of phase current stays almost constant to maintain the torque. The frequency of voltage and current also matches with the speed reference, which shows the success of the I-f open loop starting. At decreasing speed stage, the sudden drop in speed leads to a decrease of the IPMSM line-line voltage, while the inverter maintains the voltage before the current

regulators stabilize the currents. Therefore, there are some fluctuations in the current. The oscilloscope waveform is shown in Fig. 5.10. Then the voltage and current are sent to the

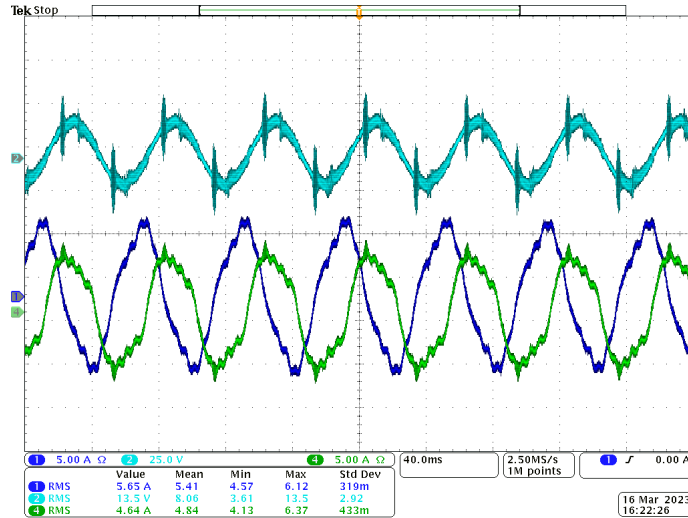


Figure 5.10: Line-line voltage and phase A, B current during I-f starting stage (The cyan curve is V_{ab} , the blue curve is I_a , the green curve is I_b)

flux linkage observer to estimate the $\lambda_{\alpha\beta}$, as shown in Fig. 5.11. The estimated λ keeps a magnitude of $0.1Wb$, while the frequency matches the speed reference. Furthermore, there is a $\frac{\pi}{2}$ phase delay between λ_α and λ_β as we expected. Furthermore, the current harmonic during the decreasing speed range also influences the flux linkage estimation.

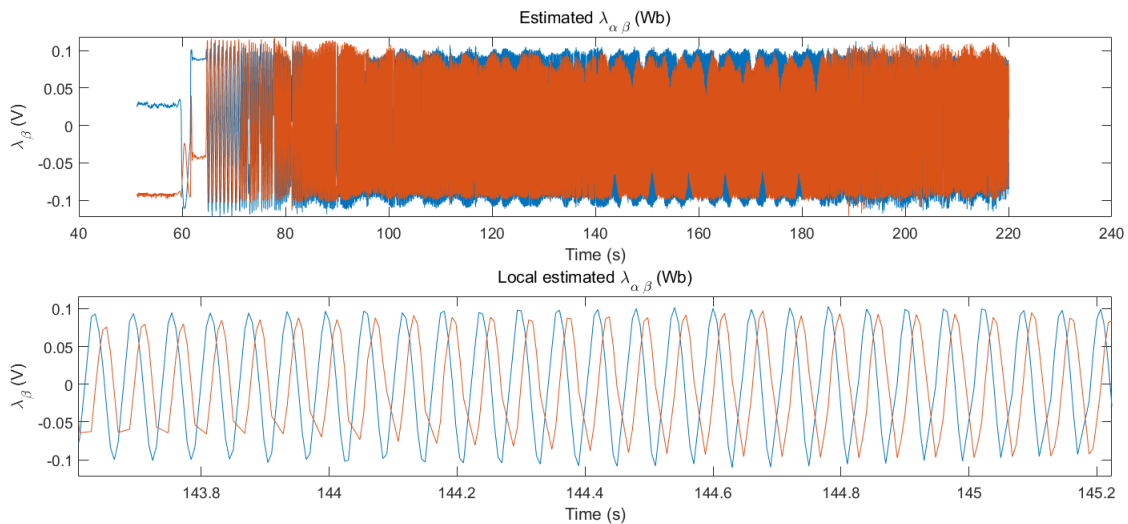


Figure 5.11: Estimated $\lambda_{\alpha\beta}$ from flux linkage observer

The estimated flux linkage contains the θ_e we need, and a phase lock loop will extract ω_e

and θ_e , as shown in Fig. 5.12. At the low-speed range, the maximum error of the estimated speed goes to 40 rpm and cannot converge to the real speed. However, when the speed is higher than 100rpm, the estimated speed can quickly converge to the real value. At 250rpm, the error of estimated speed can stay at 1 rpm and the estimated position error is almost zero. However, there are also some errors when the sudden speed change happens, and the phase lock loop needs re-tuning. In decreasing speed conditions, the harmonics in current influence the speed estimation as expected. Therefore, we should avoid the transition between open and closed-loop control during this stage.

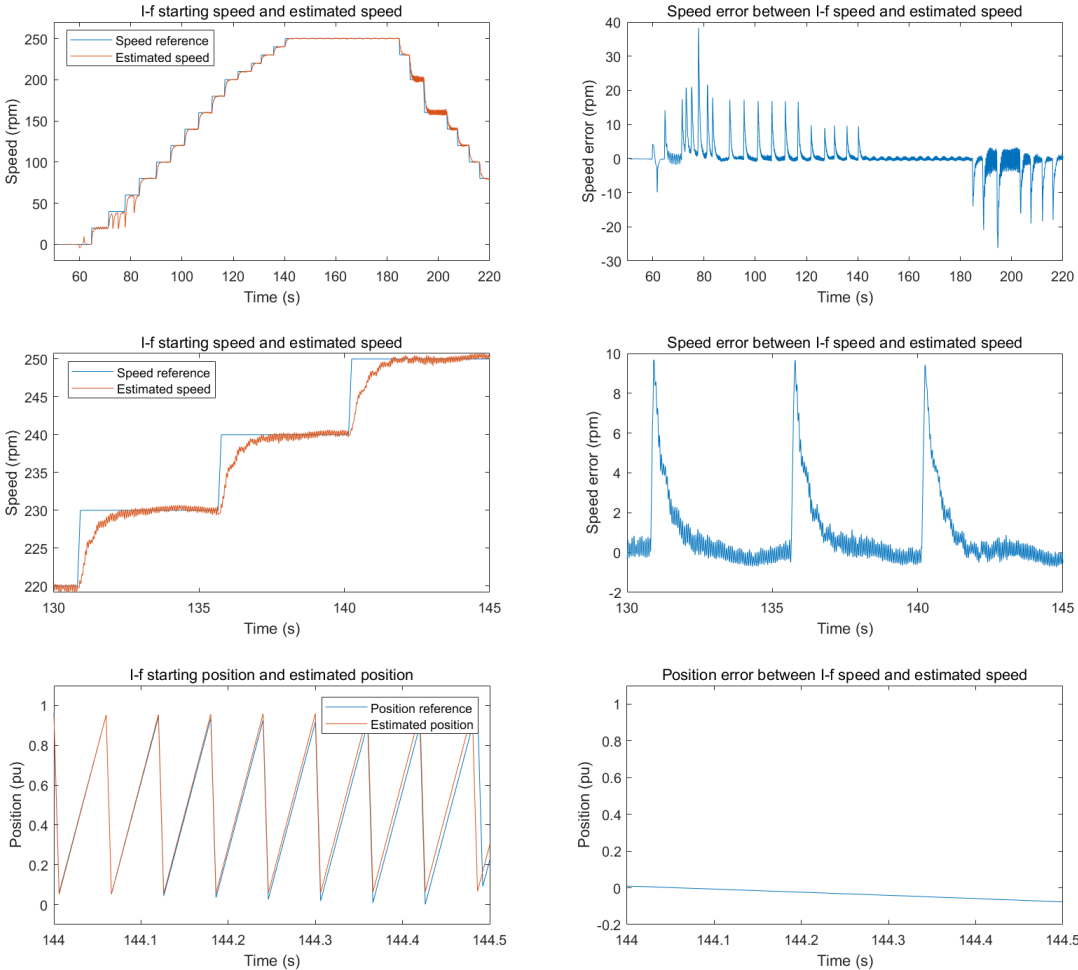


Figure 5.12: Speed (position) reference, estimated speed (position), and error

Linear increasing speed reference

The line-line voltage, phase current, and estimated $\lambda_{\alpha\beta}$ in the linear speed reference test are shown in Fig. 5.13. Similar to the step speed reference test, the voltage increases with the speed, while the current remains almost constant.

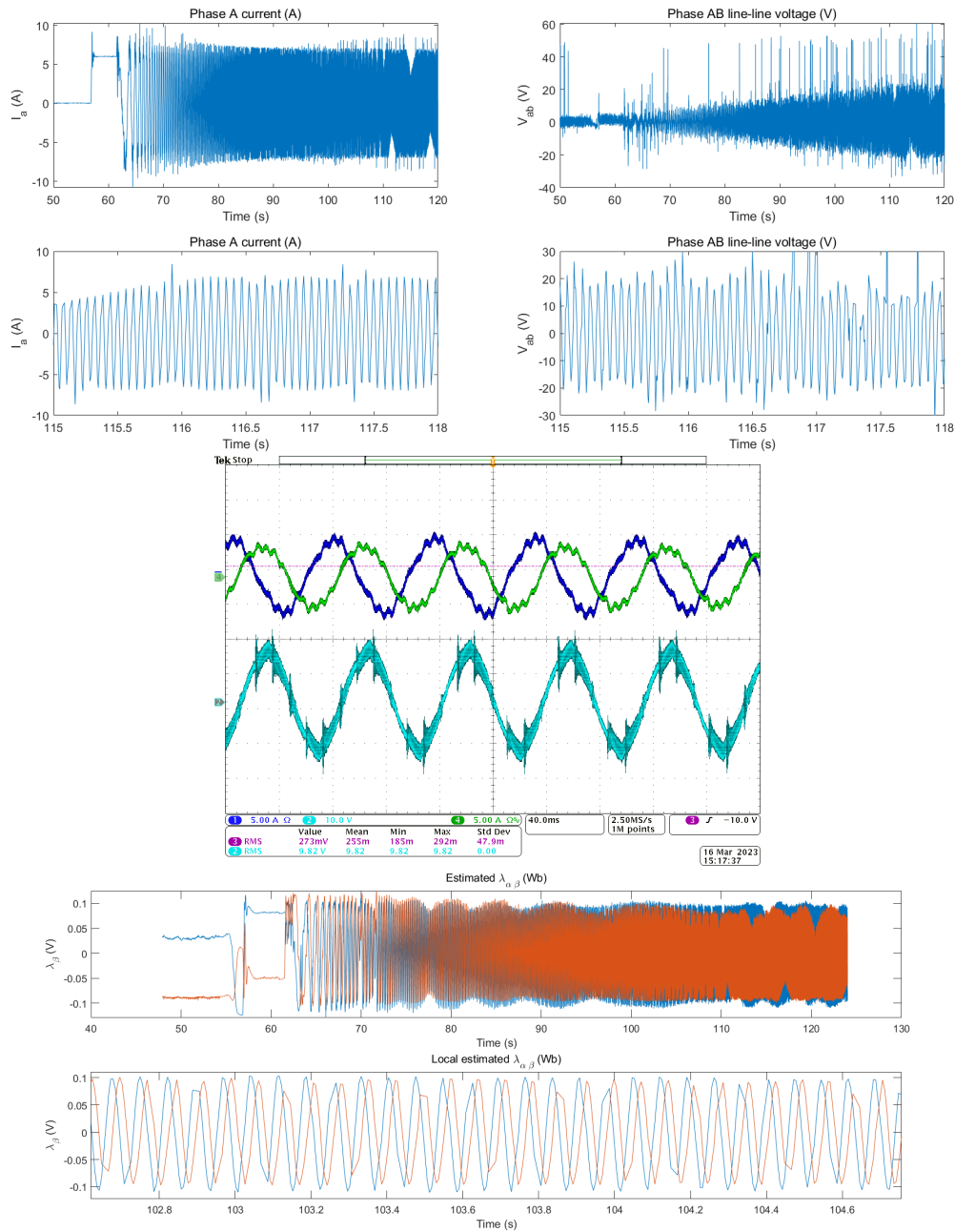


Figure 5.13: Phase current and line-line voltage at linear I-f starting stage

The estimated speed, rotor position, and their error are shown in Fig. 5.14. During the accelerating stage, the error of estimated speed stays at 3 rpm and drops to 1 rpm after the motor stabilizes at 250 rpm. However, there are still some high errors during the low-speed condition. Though there is a one-second delay between the estimated speed and the actual speed, the maximum error is 3 rpm, which can be compensated by the speed regulator [24].

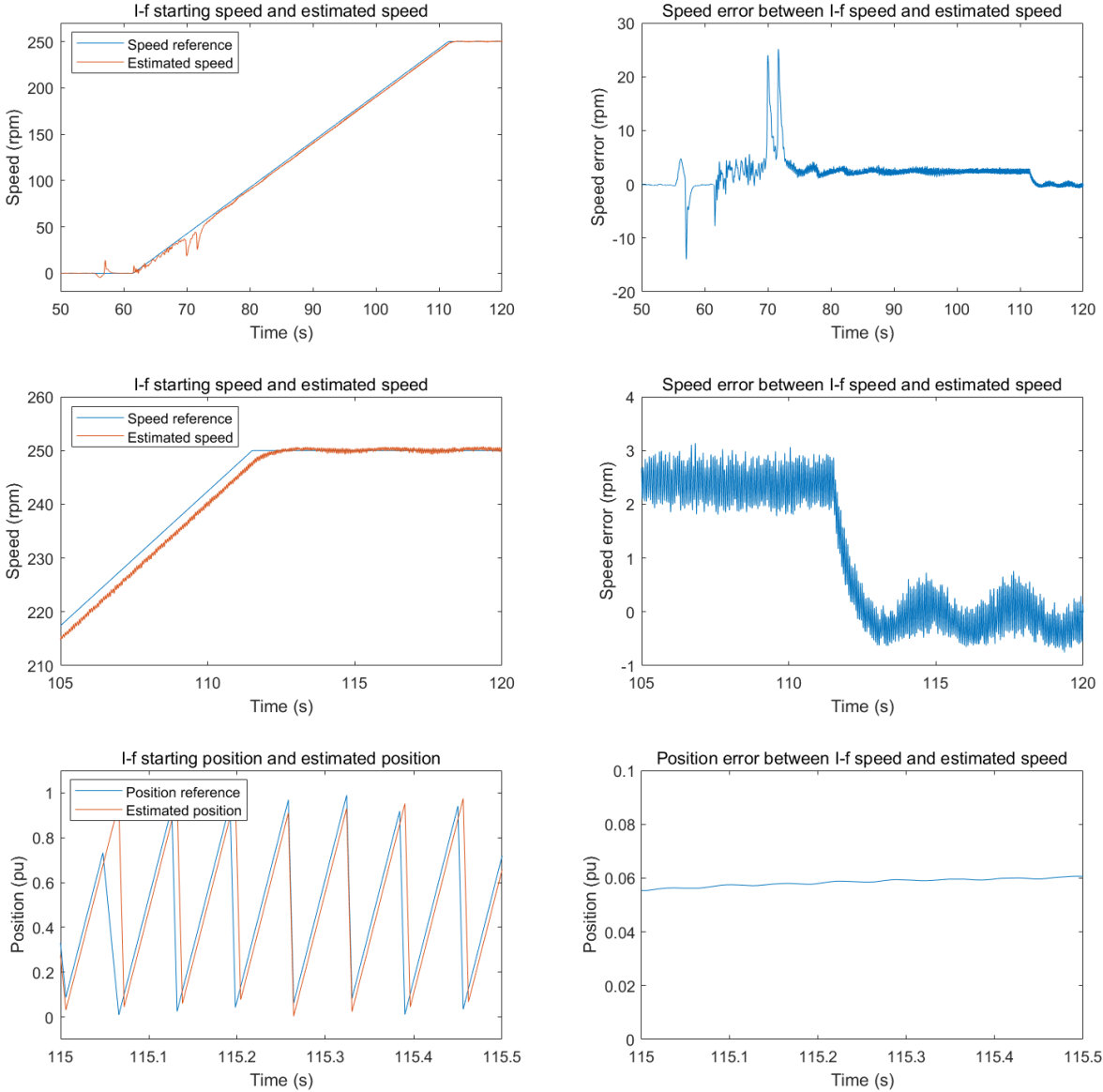


Figure 5.14: Speed (position) reference, estimated speed (position), and error

5.4 Transition and closed loop test

The smooth transition strategy between I-f open loop starting and closed loop control mentioned in chapter 4 is tested as shown in Fig. 5.15. The transition starts at 110.7s and ends at 115.2s.

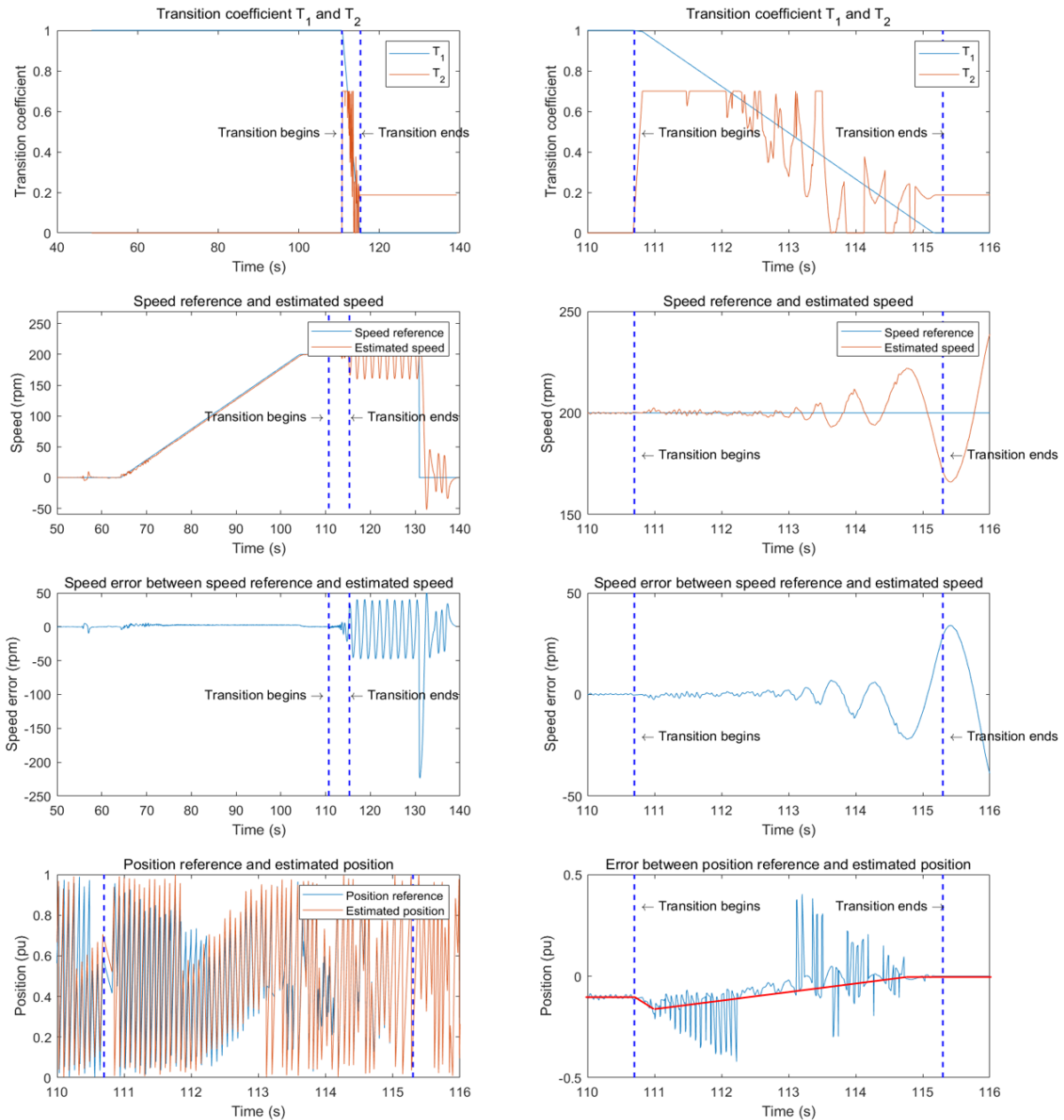


Figure 5.15: Transition coefficient, estimated speed (position), and error during transition

During the transition, transition coefficient T_1 decreases to 0 from 1, and T_2 first increases to 0.7 and stabilizes to 0.2, and the feed-forward I_{sqfft} computed by T_2 will be added to I_{sq} reference, which can compensate the friction torque. The error in rotor position estimation decreases from $0.1pu$ to 0, which proves the estimated dq axis is attracted to the real dq axis. The error in the estimated speed is less than 5 rpm during the first half of the transition. However, the speed fluctuates significantly during the transition's latter half. Furthermore, after the transition, the speed and the phase current and line-line voltage continue fluctuating, as shown in Fig. 5.16.

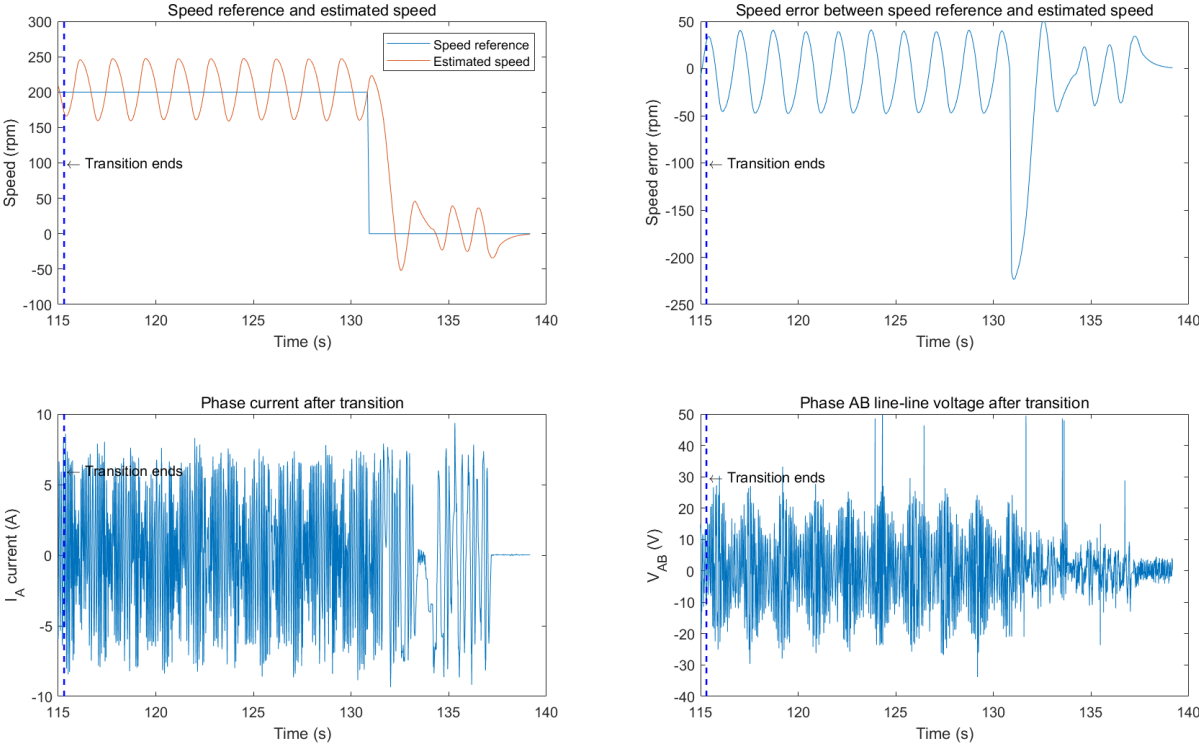


Figure 5.16: Speed and error after transition

Based on the observation of the speed curve, an intuitive guess is the bandwidth of the speed regulator is too low, which leads to controller saturation, and the saturation leads to speed fluctuation. After re-tuning the speed regulator, the speed fluctuation disappears as expected. The speed reference, estimated speed, and speed error are shown in Fig. 5.17. After the transition, the closed-loop system error can maintain in 1rpm, which proves the

successful transition from open-loop I-f starting to closed-loop control.

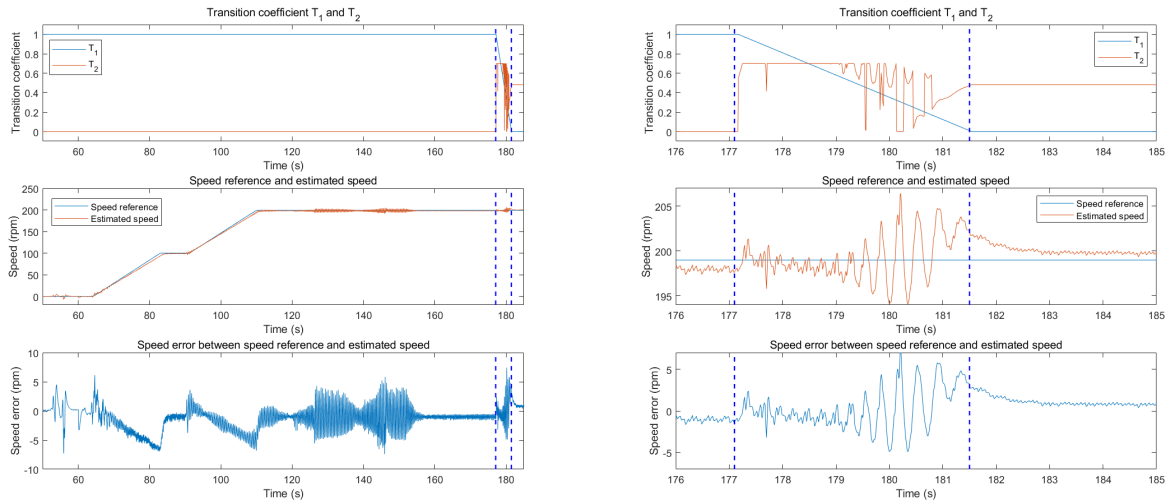


Figure 5.17: Transition coefficient, estimated speed (position), and error during transition

The closed-loop test speed and error are shown in Fig. 5.18. According to the experiment, when the speed is lower than $400rpm$, the real speed can converge to speed reference without overshooting in 1.5s. However, when speed reference is at $500rpm$ and $600rpm$, there is a

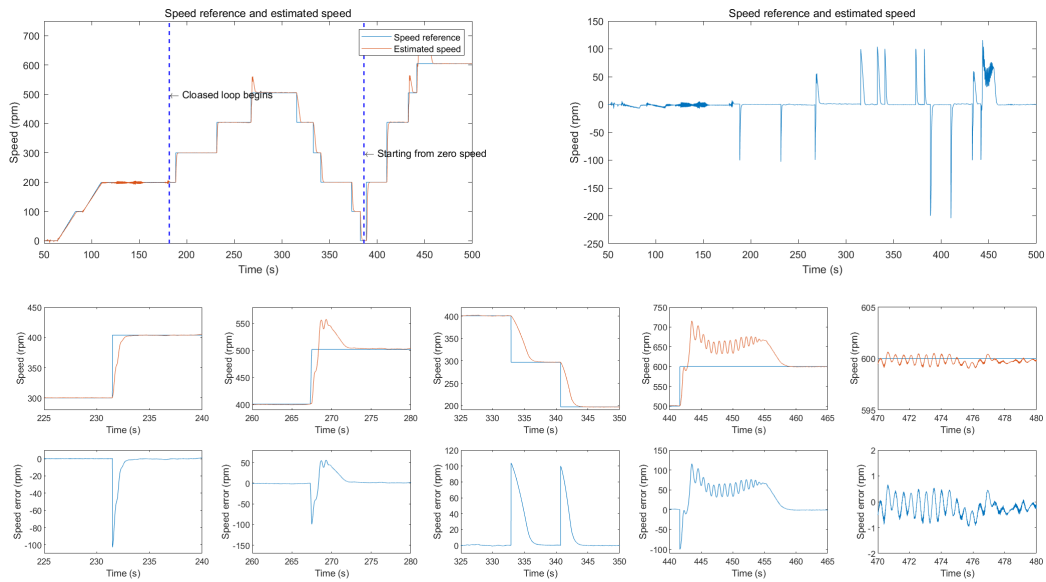


Figure 5.18: Speed and error of closed-loop test

$50rpm$ overshoot. Furthermore, because a positive $I_s d$ is continuously fed into the IPMSM to maintain alignment, the IPMSM can start from zero speed, which can be proved by the second

part of Fig. 5.18. However, if we do not give a d-axis current, the motor will lose alignment when starting from zero speed. Therefore, though the I_{sd} would generate reactive power and decrease the overall efficiency, it is still an effective strategy to start a sensorless motor system from zero speed. The oscilloscope screenshots of the motor under different speed references are shown in Fig. 5.19. When $\omega_m = 200, 300, 400, 500, 600rpm$, the fundamental frequency is $f_e = \frac{\omega_m P}{60} = 13.33, 20, 26.67, 33.33, 40Hz$, which match the current and voltage frequency from oscilloscope waveform.

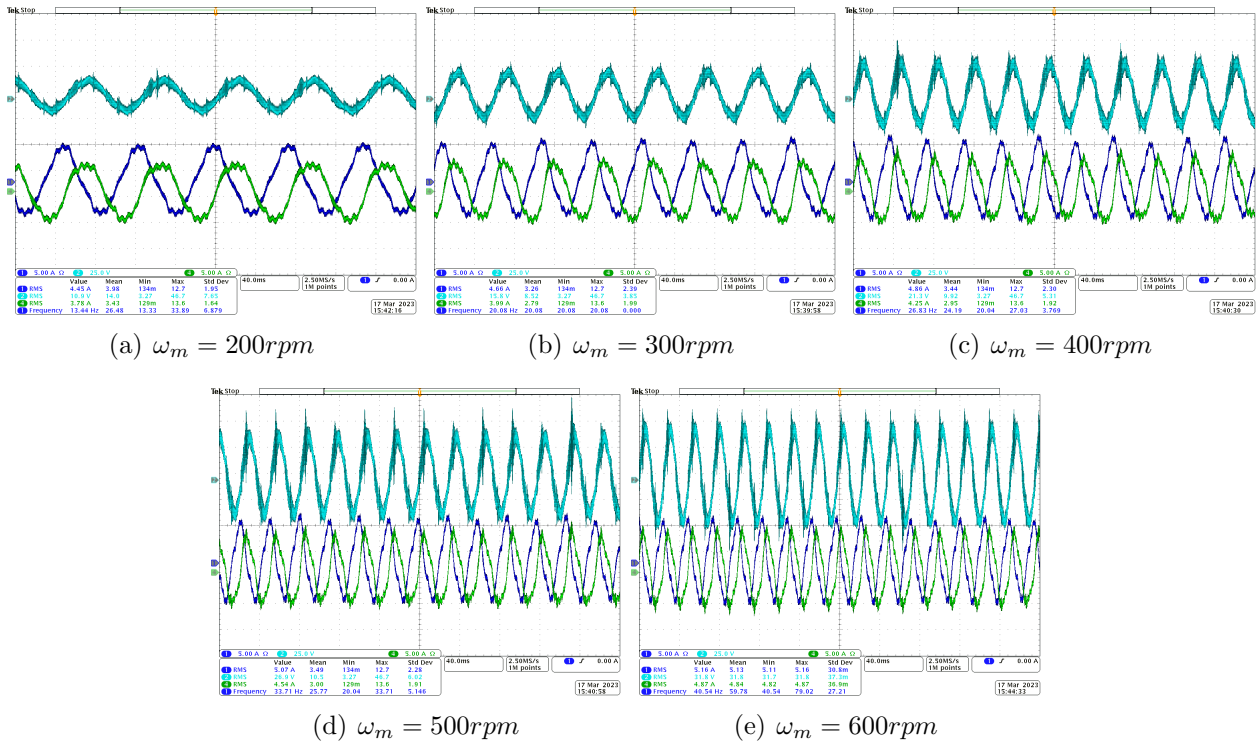


Figure 5.19: Line-line voltage V_{ab} and Phase A, B current I_a, I_b of closed-loop test (Cyan curves are V_{ab} , blue curves are I_a , green curves are I_b)

Chapter 6

Conclusions

This thesis proposed and implemented a sensorless control IPMSM system, which consists of a T-type inverter, a flux-linkage observer, and an innovative starting strategy for IPMSM. Using the flux linkage observer, the IPMSM can start and work without an encoder under 70% of rated speed. The T-type inverter is simulated in Simulink and assessed in hardware to ensure it can give sinusoidal voltage output with obviously lower THD, and with the help of the three-level SVPWM strategy, the DC link voltage utilization is significantly increased. The sensorless control IPMSM is also simulated in Simulink and tested in hardware. Under 70% of the rated speed, the speed error is less than $1rpm$, and the time response is less than $0.8s$.

Additionally, an innovative blending starting strategy from zero speed for IPMSM is proposed and tested. The blending strategy allows IPMSM starts by open-loop and transits smoothly to flux linkage observer-based closed-loop control with an error of less than $5rpm$.

Future work for this project includes: 1)adjusting flux-linkage observer architecture to increase convergence speed, which can improve low-speed condition response and accuracy, 2)adjusting the transition strategy to allow transition with varying speed, 3)re-calibrating the speed regulator to decrease full-speed overshooting, and 4)operating the system at full-speed and full-load conditions.

References

- [1] H. M. Kim, Y.-J. Kim, and S.-Y. Jung, “Torque ripple and back emf harmonic reduction of ipmsm with asymmetrical stator design,” in *2017 20th International Conference on Electrical Machines and Systems (ICEMS)*, IEEE, 2017, pp. 1–4.
- [2] Z. Zhang, “Sensorless control of synchronous machines using fundamental back-emf voltage—a review,” *IEEE Transactions on Power Electronics*, 2022.
- [3] Z. Yin, Y. Zhang, X. Cao, D. Yuan, and J. Liu, “Estimated position error suppression using novel pll for ipmsm sensorless drives based on full-order smo,” *IEEE Transactions on Power Electronics*, vol. 37, no. 4, pp. 4463–4474, 2021.
- [4] J. Liu and Y. Zhang, “Performance improvement of nonlinear flux observer for sensorless control of pmsm,” *IEEE Transactions on Industrial Electronics*, 2023.
- [5] Y. Zhang and R. Qi, “Flux-weakening drive for ipmsm based on model predictive control,” *Energies*, vol. 15, no. 7, p. 2543, 2022.
- [6] J. Chen, Y. Fan, W. Wang, C. H. Lee, and Y. Wang, “Sensorless control for synrm drives using a pseudo-random high-frequency triangular-wave current signal injection scheme,” *IEEE Transactions on Power Electronics*, vol. 37, no. 6, pp. 7122–7131, 2022.
- [7] V. T. Ha, P. T. Giang, and V. H. Phuong, “T-type multi-inverter application for traction motor control,” *Engineering, Technology & Applied Science Research*, vol. 12, no. 2, pp. 8321–8327, 2022.

- [8] L. Xie and J. Yao, "Common-mode voltage reduction and neutral point voltage balance modulation technology of quasi-z-source t-type three-level inverter," *Electronics*, vol. 11, no. 14, p. 2203, 2022.
- [9] E. Serban, M. Ordonez, and C. Pondiche, "Dc-bus voltage range extension in 1500 v photovoltaic inverters," *IEEE Journal of Emerging and Selected Topics in Power Electronics*, vol. 3, no. 4, pp. 901–917, 2015.
- [10] U.-M. Choi, F. Blaabjerg, and K.-B. Lee, "Reliability improvement of a t-type three-level inverter with fault-tolerant control strategy," *IEEE Transactions on Power Electronics*, vol. 30, no. 5, pp. 2660–2673, 2014.
- [11] M. Sajitha and R. Ramchand, "Space vector pwm scheme for three phase three level t-type npc inverter," in *2019 2nd International Conference on Intelligent Computing, Instrumentation and Control Technologies (ICICT)*, IEEE, vol. 1, 2019, pp. 523–528.
- [12] Y. Tang, X. Li, S.-Z. Zhou, C. Sun, and G. Chen, "Comprehensive study of fast load modulation with volt-second balance in a dual-active-bridge converter," *IET Power Electronics*, vol. 12, no. 6, pp. 1357–1367, 2019.
- [13] C. Wu, Y. Zhao, and M. Sun, "Enhancing low-speed sensorless control of pmsm using phase voltage measurements and online multiple parameter identification," *IEEE Transactions on Power Electronics*, vol. 35, no. 10, pp. 10 700–10 710, 2020.
- [14] M. Liserre, F. Blaabjerg, and S. Hansen, "Design and control of an lcl-filter-based three-phase active rectifier," *IEEE Transactions on industry applications*, vol. 41, no. 5, pp. 1281–1291, 2005.
- [15] A. A. Deshpande, "Design of three level silicon carbide neutral point clamped inverter," Ph.D. dissertation, The University of Texas at San Antonio, 2019.
- [16] E. Hendawi, F. Khater, A. Shaltout, and G. Egypt, "Analysis, simulation and implementation of space vector pulse width modulation inverter," *Power*, vol. 4, no. T6, T2, 2006.

- [17] J. Lee, J. Hong, K. Nam, R. Ortega, L. Praly, and A. Astolfi, “Sensorless control of surface-mount permanent-magnet synchronous motors based on a nonlinear observer,” *IEEE Transactions on power electronics*, vol. 25, no. 2, pp. 290–297, 2009.
- [18] L. Ding, Y. W. Li, and N. R. Zargari, “Discrete-time smo sensorless control of current source converter-fed pmsm drives with low switching frequency,” *IEEE Transactions on Industrial Electronics*, vol. 68, no. 3, pp. 2120–2129, 2020.
- [19] D. Liang, J. Li, and R. Qu, “Sensorless control of permanent magnet synchronous machine based on second-order sliding-mode observer with online resistance estimation,” *IEEE Transactions on Industry Applications*, vol. 53, no. 4, pp. 3672–3682, 2017.
- [20] G. Chen and L. Xu, “Adaptive quasi-proportional resonant control with parameter estimation for pmsm sensorless control,” *Advances in Mechanical Engineering*, vol. 15, no. 2, p. 16 878 132 231 154 069, 2023.
- [21] X. Ding and Z. Liu, “Position sensorless control and real-time commutation delay compensation of a micro bldc motor,” in *2022 IEEE Transportation Electrification Conference and Expo, Asia-Pacific (ITEC Asia-Pacific)*, IEEE, 2022, pp. 1–5.
- [22] H. Yan, W. Wang, Y. Xu, and J. Zou, “Position sensorless control for pmsm drives with single current sensor,” *IEEE Transactions on Industrial Electronics*, vol. 70, no. 1, pp. 178–188, 2022.
- [23] Q. Tang, D. Chen, and X. He, “Integration of improved flux linkage observer and i–f starting method for wide-speed-range sensorless spmsm drives,” *IEEE Transactions on Power Electronics*, vol. 35, no. 8, pp. 8374–8383, 2019.
- [24] W. Chen, Z. Liu, Y. Cao, X. Li, T. Shi, and C. Xia, “A position sensorless control strategy for the bldcm based on a flux-linkage function,” *IEEE Transactions on Industrial Electronics*, vol. 66, no. 4, pp. 2570–2579, 2018.

Appendix A

PCB prototype of the T-type inverter

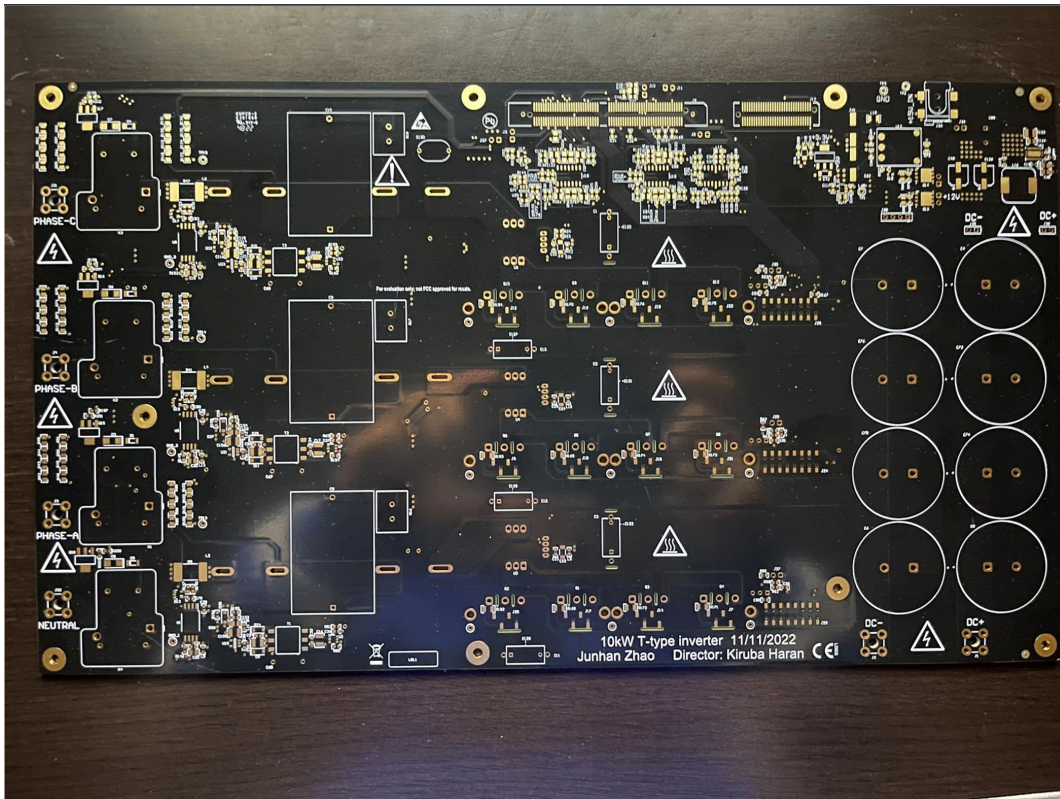


Figure A.1: Front face of the PCB prototype

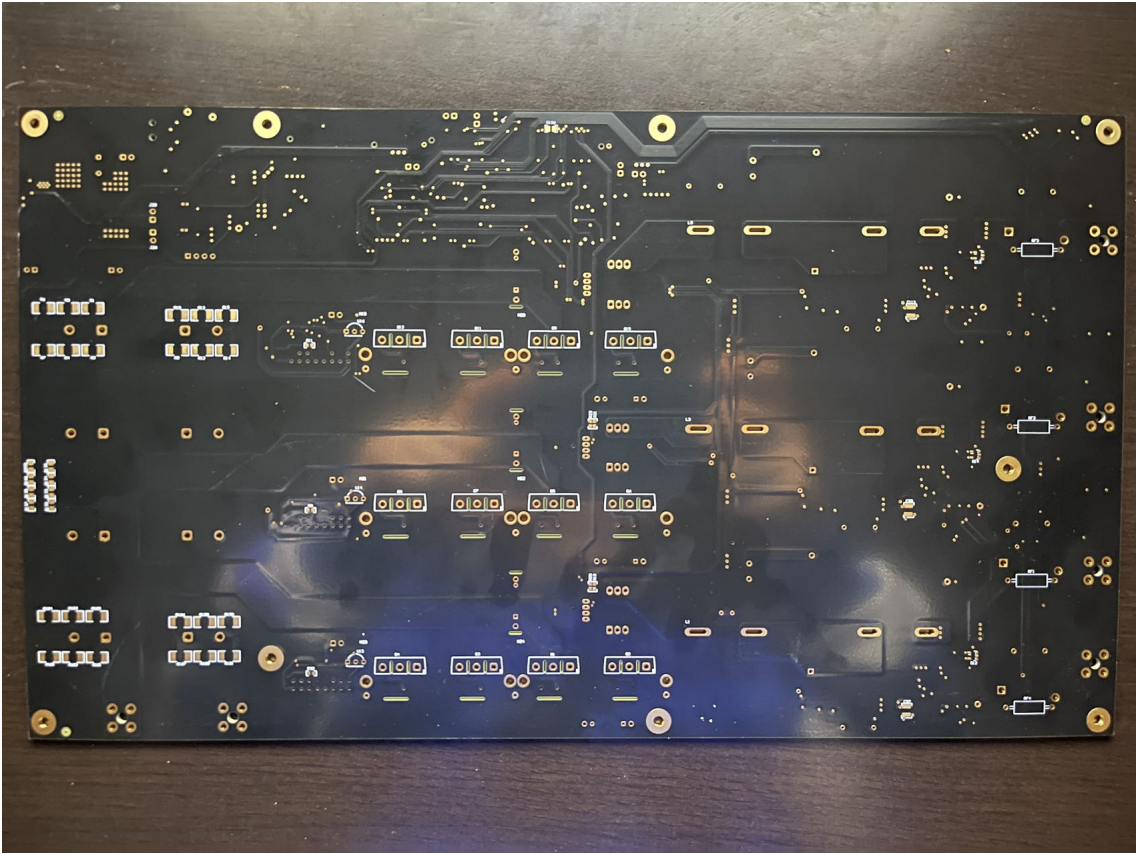


Figure A.2: Back face of the PCB prototype